

# UC Santa Cruz

## UC Santa Cruz Electronic Theses and Dissertations

### Title

CuO Thin Film Crystallization by Chevron CW Laser Annealing

### Permalink

<https://escholarship.org/uc/item/0ct2f3s5>

### Author

Losakul, Ravipa

### Publication Date

2018

Peer reviewed|Thesis/dissertation

UNIVERSITY of CALIFORNIA  
SANTA CRUZ

**CuO THIN FILM CRYSTALLIZATION BY  
CHEVRON CW LASER ANNEALING**

A thesis submitted in partial satisfaction  
of the requirements for the degree of

MASTER OF SCIENCE

in

ELECTRICAL ENGINEERING

by

**Ravipa Decharit Losakul**

December 2018

The Thesis of Ravipa Decharit Losakul is approved:

---

Professor Nobuhiko Kobayashi, Chair

---

Professor Sara Abrahamsson

---

David Fryauf

---

Lori Kletzer

Vice Provost and Dean of Graduate Studies

Copyright © by Ravipa Decharit Losakul

2018

# Contents

List of Figures.....	iii
List of Tables.....	vi
Abstract.....	vii
Acknowledgements.....	viii
<b>I. Introduction.....</b>	<b>1</b>
<b>1.1 Thin Films.....</b>	<b>1</b>
<b>1.2 RF Magnetron Sputtering Deposition.....</b>	<b>10</b>
<b>1.2.1 Sputtering Process.....</b>	<b>10</b>
<b>1.3 Chevron CW Laser Annealing.....</b>	<b>11</b>
<b>II. Procedure.....</b>	<b>14</b>
<b>III. Results.....</b>	<b>16</b>
<b>3.1 Post Deposition Characterization: Ellipsometry.....</b>	<b>17</b>
3.1a Sample A	
3.1b Sample B	
3.1c Sample C	
<b>3.2 Post Deposition Characterization: Atomic Force Microscopy (AFM)</b>	
3.2a Bare Quartz Reference <sup>33</sup>	
3.2b Sample A	
3.2c Sample B	
3.2d Sample C	
<b>3.3 Post Deposition Crystallization.....</b>	<b>49</b>
<b>IV. Conclusion.....</b>	<b>53</b>
<b>V. References.....</b>	<b>55</b>

# List of Figures

<b>Figure 1</b>	Diagram of atomic surface processes and energies of thin film growth.....	4
<b>Figure 2</b>	Coalescence by Ostwald ripening, Mobility of Islands and Growth.....	5
<b>Figure 3</b>	Volmer-Weber, Frank-van der Merwe, and Stranski-Krastanov.....	5
<b>Figure 4</b>	Epitaxial Interface Between Materials A & B.....	7
<b>Figure 5</b>	Mismatched Epitaxial Interface Between Materials A & B.....	7
<b>Figure 6</b>	Schematic Diagram of Chevron Tipped Laser Beam.....	12
<b>Figure 7</b>	Diagram Chevron Annealing System & Tip Irradiation Images.....	13
<b>Figure 8</b>	Sputtering System & Covered Sputtering Targets.....	15
<b>Figure 9</b>	Ignited Plasma Under Target Shutter.....	15
<b>Figure 10</b>	Sample A- Measurement 1 - Reflection/Psi/Delta Values.....	21
<b>Figure 11</b>	Sample A – Measurement 1 - n-k values.....	21
<b>Figure 12</b>	Sample A- Measurement 2 - Reflection/Psi/Delta Values.....	22
<b>Figure 13</b>	Sample A – Measurement 2 - n-k values.....	22
<b>Figure 14</b>	Sample A- Measurement 3 - Reflection/Psi/Delta Values.....	23
<b>Figure 15</b>	Sample A – Measurement 3 - n-k values.....	23
<b>Figure 16</b>	Sample B- Measurement 1 - Reflection/Psi/Delta Values.....	25
<b>Figure 17</b>	Sample B – Measurement 1 - n-k values.....	25
<b>Figure 18</b>	Sample B- Measurement 2 - Reflection/Psi/Delta Values.....	26
<b>Figure 19</b>	Sample B – Measurement 2 - n-k values.....	26
<b>Figure 20</b>	Sample B- Measurement 3 - Reflection/Psi/Delta Values.....	27
<b>Figure 21</b>	Sample B – Measurement 3 - n-k values.....	27

<b>Figure 22</b> Sample C – Measurement 1 - Reflection/Psi/Delta Values.....	29
<b>Figure 23</b> Sample C – Measurement 1 - n-k values.....	29
<b>Figure 24</b> Sample C – Measurement 2 - Reflection/Psi/Delta Values.....	30
<b>Figure 25</b> Sample C – Measurement 2 - n-k values.....	30
<b>Figure 26</b> Sample C – Measurement 3 - Reflection/Psi/Delta Values.....	31
<b>Figure 27</b> Sample C – Measurement 3 - n-k values.....	31
<b>Figure 28</b> AFM Topography Images of Bare Quartz Reference .....	34
<b>Figure 29</b> AFM Topography Images of Sample A - 1 $\mu$ m.....	35
<b>Figure 30</b> AFM Topography Images of Sample A - 10 $\mu$ m.....	36
<b>Figure 31</b> AFM Topography Images of Sample B – 1 $\mu$ m.....	37
<b>Figure 32</b> AFM Topography Images of Sample B - 10 $\mu$ m.....	38
<b>Figure 33</b> AFM Topography Images of Sample C - 1 $\mu$ m.....	39
<b>Figure 34</b> AFM Topography Images of Sample C - 10 $\mu$ m.....	39
<b>Figure 35</b> Magnified Image of Sample A[b] - 1 $\mu$ m.....	43
<b>Figure 36</b> Magnified Image of Sample B[b] - 1 $\mu$ m.....	43
<b>Figure 37</b> 3D Image of Bare Quartz Reference [b] - 1 $\mu$ m.....	44
<b>Figure 38</b> 3D Image of Sample A [b] - 1 $\mu$ m.....	44
<b>Figure 39</b> 3D Image of Sample B [b] - 1 $\mu$ m.....	45
<b>Figure 40</b> 3D Image of Sample C [b] - 1 $\mu$ m.....	45
<b>Figure 41</b> Total Laser Annealing of Sample B.....	50
<b>Figure 42</b> Magnified Laser Annealing of Sample B with Ablation.....	50

<b>Figure 43</b> Laser Annealing of Sample C.....	51
<b>Figure 44</b> Magnified Laser Annealing of Sample C.....	52
<b>Figure 45</b> Surface Irradiation of Chevron-Tipped Laser Beam for Sample B &..... Sample C	52

# List of Tables

<b>Table 1</b> Sample A Deposition Parameters.....	16
<b>Table 2</b> Sample B Deposition Parameters.....	16
<b>Table 3</b> Sample C Deposition Parameters.....	17
<b>Table 4</b> Sample A - Film Thickness, Roughness and RMSE Values.....	20
<b>Table 5</b> Sample A – Refractive Index and Extinction Coefficient.....	20
<b>Table 6</b> Sample B - Film Thickness, Roughness and RMSE Values.....	24
<b>Table 7</b> Sample B – Refractive Index and Extinction Coefficient.....	24
<b>Table 8</b> Sample C - Film Thickness, Roughness and RMSE Values.....	28
<b>Table 9</b> Sample C – Refractive Index and Extinction Coefficient.....	28
<b>Table 10</b> Bare Quartz Reference.....	34
<b>Table 11</b> Sample A 1 $\mu\text{m}$ .....	35
<b>Table 12</b> Sample A 10 $\mu\text{m}$ .....	36
<b>Table 13</b> Sample B 1 $\mu\text{m}$ .....	37
<b>Table 14</b> Sample B 10 $\mu\text{m}$ .....	38
<b>Table 15</b> Sample C 1 $\mu\text{m}$ .....	39
<b>Table 16</b> Sample C 10 $\mu\text{m}$ .....	40
<b>Table 17</b> Comparison of Roughness and Thickness Values. .... of Ellipsometry and AFM	48

## **Abstract**

### **CuO Thin Film Crystallization by Chevron CW Laser Annealing**

**Ravipa Losakul**

In efforts to parallel the vastly changing consumer market of electronic products, devices engineered from improved techniques in maximizing performance while minimizing loss are researched and implemented. We report the results of crystallization of CuO amorphous thin films on quartz and silicon wafers with the chevron-tipped laser annealing system. Post-deposition averaged thickness values were reported to be 3.84nm, 15.49nm, and 98.19nm for Sample A, B and C, whereas averaged roughness values were 0.43nm, 0.51nm and 4.45nm, respectively, and confirming the smoothness of an amorphous film. Additional samples were sent to be characterized and potentially crystallized by a chevron-tipped laser annealing systems. The initial results showed a laser trace of ablation on Samples B and C at a power of approximately 318mW and 120 mW, respectively. However, further results, including crystallization and analysis are incomplete.

## **Acknowledgements**

I would like to thank my research advisor, Professor Nobuhiko Kobayashi for giving me the opportunity to further explore my research interests in the NECTAR Lab. I am grateful and beyond thankful for his support and encouragement during my time as a Masters student. In addition, I would also like to thank David Fryauf for always being willing and present for all of my questions during lab and for being the wonderful role model and mentor. Furthermore, thank you to Professor Sara Abrahamson for being an amazing example of a woman in science I hope to be one day.

## **I. Introduction**

In modern day applications ranging from solar energy devices to transistors, the growth and crystallization of single-crystalline thin films on amorphous materials have become an important factor in maximizing performance and minimizing loss. Performance values such as open circuit voltage, high speed response or material and power consumption dictate the need for thoroughly investigated techniques and materials within academic and industry research efforts to parallel the rapidly changing consumer product tastes. These consumer products benefit from the improved techniques in manufacturing devices such as three-dimensional integrated circuits (3D-ICs), pixel-switching transistors and peripheral circuits for displays. Specifically, thin film deposition and crystallization techniques are modified and implemented to result in an updated innovative standard with the motivation of single-crystalline thin film growth on an amorphous surface.

### **1.1 Thin Films**

As a microscopically thin layer of material deposited onto a metal, ceramic or semi-conductive base, the production of thin films is the foundation to many electronic devices and applications. Separate from bulk materials, thin films are under constant stress and are strongly influenced by surface and interface effects. The growth of thin films is dependent on a few factors that occur in several stages during deposition.

At the earliest stage, adsorption, an approaching atom is either reflected from or physically absorbed to the substrate surface. To be absorbed, a depositing atom must

possess enough thermal energy to overcome the adsorption potential. This energy potential is described as

$$\exp \frac{-E_{des}}{kT}$$

where  $E_{des}$  is the energy barrier for desorption,  $k$  is Boltzmann constant and  $T$  is temperature. If absorbed, an atom is trapped in the surface potential and will undergo additional individual atomic processes on the substrate surface: surface diffusion/interdiffusion, re-evaporation, nucleation and subsequently, growth modes to a continuous film growth.

Surface diffusion is a thermally promoted process where depositing atoms jump around and migrate to neighboring adsorption sites on the surface. Important for nucleation, diffusion allows for depositing atoms to form clusters in different growth modes dependent on separate thermodynamic situations. The probability of an atom successfully diffusing to a permanent lattice site is dependent on temperature,  $T$ , and the diffusion energy,  $E_{diff}$ . This relation is described as the diffusion rate is

$$D = v e^{-\frac{E_{diff}}{kT}}$$

and the diffusion length is known as

$$\Lambda = a\sqrt{(k_s t)}$$

At lower temperatures, the diffusion length increases with temperature. At high temperatures, the desorption rate increases, taking over adsorption and decreases diffusion length.

Otherwise known as desorption, re-evaporation occurs when the atom possesses more energy than the surface potential barrier. As characterized by time,  $\tau$ , the rate of desorbing atoms is given by

$$\frac{n_{des}}{n_{ads}} = \nu \exp^{-E_{des}/T}$$

where  $n_{des}$  is the number of desorbing atoms,  $n_{ads}$  is the number of adsorbing atoms, and  $\nu$  is the frequency of atoms attempting to escape the surface.  $\nu$  is typically assumed to be the vibrating lattice frequency of the material.

Nucleation occurs when a diffusing atom remains trapped within the material's surface potential and begins interacting with neighboring atoms to form organized clusters. By incorporating trapped surface atoms, nucleated clusters continue to grow in size and exhibit bulk properties like surface tension and latent heat. While dependent on the relation between Gibbs free energy and the surface energy, clusters of radius,  $r$ , populate the surface towards a density equilibrium described as

$$\frac{n(r)}{n_{ads}} = \exp \left[ \frac{-\Delta G(r)}{kT} \right]$$

where  $\Delta G(r)$  is the Gibbs free energy of cluster formation of radius  $r$  and  $n(r)$  is the number of atoms at radius  $r$ . It is important to note that this relation is valid for any radius under the critical radius: the threshold of nucleation and the point where film growth initiates on a substrate. For every atom incorporated to a cluster before critical radius, Gibbs free energy would increase while compensating surface energy. However, after reaching critical size, every additional atom will decrease Gibbs free energy and overcompensates the need for increased surface energy [1].

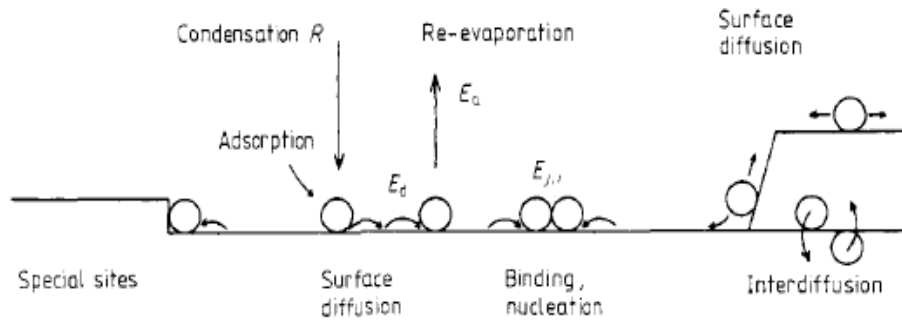


**Figure 1** Diagram of atomic surface processes and energies of thin film growth [2]

Adsorbed atoms naturally diffuse across the surface until it is lost to either re-evaporation or nucleation. Once atom clusters reach their critical size, nucleation no longer occurs and the clusters form into islands. The rate of island growth is dependent on the rate of incorporated adsorbed atoms, but its also limited by surface diffusion and interface transfer. Eventually, neighboring islands merge together to minimize surface energy as coalescence.

While dependent on substrate temperature and respective surface energies, coalescence occurs in three ways: Ostwald ripening, mobility of islands and island growth; as depicted in Figure 2. Ostwald ripening occurs under the vapor pressure differences of two nuclei; where a larger nucleus increases in size at the expense of a smaller nucleus. Mobility of islands occurs with smaller islands, and their larger mobility, incorporating themselves into larger surrounding islands. Growth of islands occurs with neighboring islands incorporate each other into a single unit, either by retaining their shape or morphing into a collective island. Depending on several factors, islands will exhibit

characteristics from three growth modes: Volmer-Weber (Island), Stranski-Krastanov (Layer Plus Island), Frank-van der Merwe (Layer); as depicted in Figure 3.

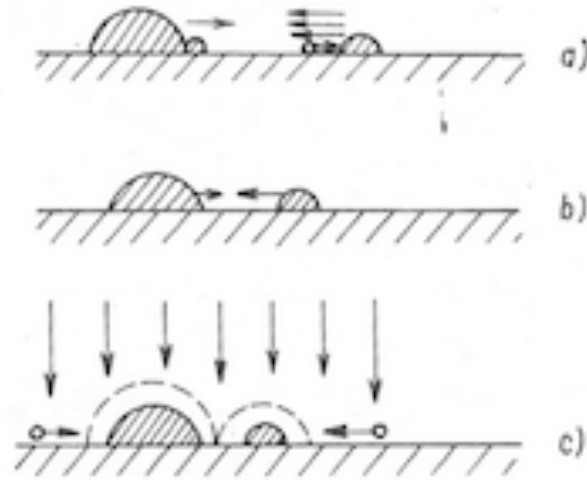


**Figure 2** Coalescence by (a) Ostwald ripening, (b) Mobility of Islands and (c) by Growth [3]

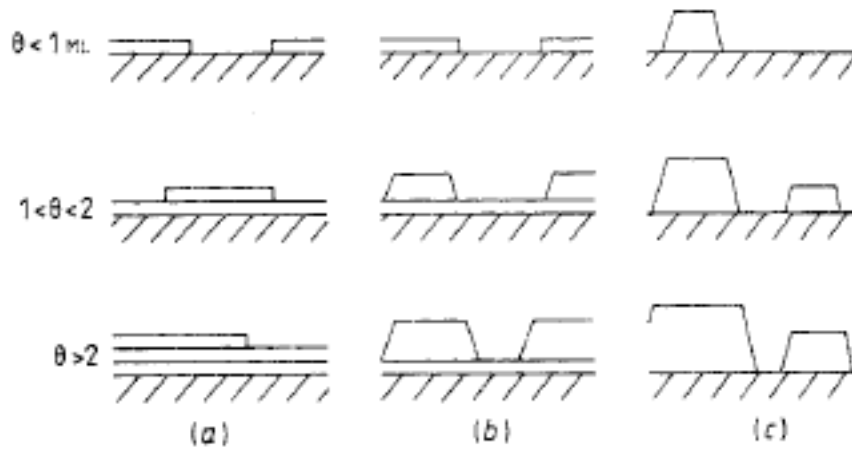


**Figure 3** Volmer-Weber (island), Frank-van der Merwe (layer) and Stranski-Krastanov (layer plus island). [2]

As the adsorbed atoms continue to collect to form nuclei, the final stages of film growth occur with crystallization. From coalescence, islands reach atomic equilibrium through surface and volume diffusion over a period of time. The critical stage for crystallization occurs when the amount of time for coalescence boundary removal equals the amount of time for a growing island to interact with its nearest neighboring island. Since the physical properties of a thin film are dependent on the final film structure, its formation and specific influencing factors are important to briefly discuss [4].

### **Thin Film Structure, Factors and Defects**

Due its molecular nature, the purity of single-crystalline thin films on amorphous materials have been elusive due to mismatch lattice structures and difficulty in controlling growth direction. Traditionally, epitaxial growth techniques like metal-organic chemical vapor deposition (MOCVD) or molecular beam epitaxy (MBE) are used to produce single-crystalline thin films, however, they require materials that contain closely matched lattice structures. Ideal crystalline growth occurs when both material structures contain the same lattice constant and maintain a low energy atomic configuration, as seen in Figure 4. Although this low-energy configuration is preferred in nature, a perfect crystalline structure at lower temperature limits are relatively immobile; restricting its potential properties to be utilized in various electronic devices. The materials' respective properties, values and variety would be restricted solely to their composition and crystal structure [5].

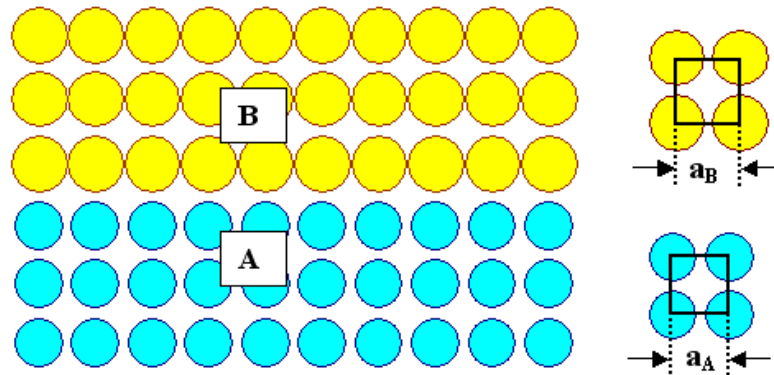


**Figure 4** Epitaxial Interface Between Materials A & B [5]

As the shortcoming of an imperfect crystal lattice, impurities are a contributing factor to film growth and are utilized to create diverse combinations. Deposited materials with slightly different lattice constants allows for properties, like electrical or mechanical, to be developed across a wide variety of devices. Impurities are established through strain and stress energies, as deposited atoms are squeezed to match with its intended substrate, as highlighted in Figure 5. Under stress, several types of film defects are most likely to occur and are indexed across spatial dimensions and are briefly discussed.

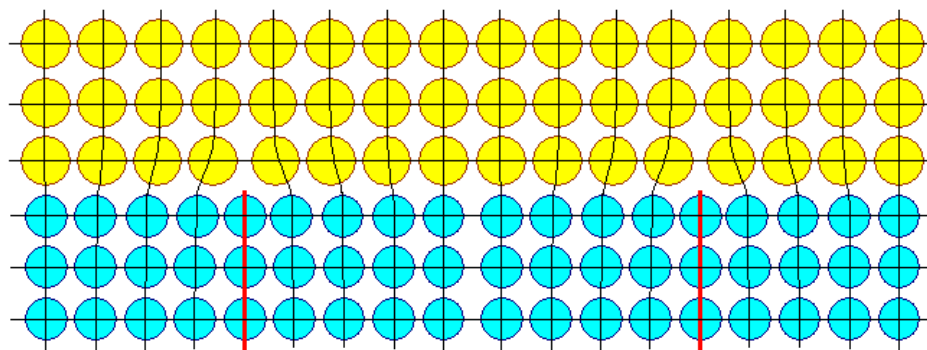


**Figure 5** Mismatched Epitaxial Interface Between Materials A & B [5]

Zero dimensional defects are more commonly known as point defects and are either intrinsic or extrinsic. Intrinsic defects occur within the lattice as either a vacancy or interstitial. Vacancies occur when an atom is missing from its delegated site, whereas interstitials has an atom occupies a site where no other atom would ordinarily occupy. Extrinsic defects, depending on its intention, are foreign atoms classified as either solutes or impurities, with both either occupying lattice or interstitial sites. All point defects affect engineering properties and are purposely used to control electrical properties, such as the concentration type of charge carriers.

Either occurring during the growth phase or interface structures, one dimensional defects are linear and occur as dislocations, where the microstructure of a crystal is deformed. The different types of dislocation include edge, screw, and mixed. Edge dislocations occur when there is a linear discontinuity between two sections of material. In the process of connecting the separated sections, excess material gathers and creates the linear defect at the point of reconstruction. Screw dislocations occur through the length of the material and causes plastic deformation. Mixed dislocations occur with dislocations at a curved “intermediate angle to the local direction of the dislocation line” and changes continuously with length [6].

Two dimensional defects appear within the interfaces of a structure as free surfaces, inter-crystalline boundaries and internal defects. Free surfaces are the external interfaces between crystalline solids and transitioning phase vapors. With the surface of the solid influenced by the interacting vapors, its structure is reconfigured with bond

interactions and chemical changes. Inter-crystalline boundaries are internal interfaces that separate grains or distinct solid phases.

Three dimensional defects materialize either as precipitates, dispersants, inclusions or voids. Precipitates are introduced into a structure as a modification through solid state reactions. As small particles, they act as obstructions to the motion of dislocations and strengthen its surrounding structure. Dispersants act as larger precipitates or grains and influence mechanical strength and electrical conductivity of the structure. Inclusions are mainly undesirable foreign particles that interfere and alter material properties. With similar effects to inclusions, voids are trapped gasses during solidification or vacancy condensation and decrease mechanical strength by promoting fractures sites.

With the multiple sources of film defects outlined, surface impurities provide a substantial influence during film growth itself. While it does provide positive modifications, the amount of impurities can have the opposite effect. As the binding energy between depositing atoms and the substrate surface is influenced by impurities, the subsequent nuclei size and growth conditions are altered. After film growth, its adhesion to the substrate becomes weaker as the bonds between film and substrate are modified to consist only of van der Waals forces. Consequently, the impurities can act as a contamination to modify film properties and are solidified during the deposition process [6]. Depending on the deposition method, the energy of impinging particles can impact the type of impurities that occur. Within this thesis, radio-frequency magnetron sputtering deposition is discussed and utilized for the film growth experiment.

## **1.2 RF Magnetron Sputtering Deposition**

A type of physical vapor deposition (PVD), sputtering deposition is a process where particles are ejected from a solid target material through bombardment of energetic particles. Depending on the target material, different sputtering techniques can be used for film deposition. Used with non-dielectric materials, RF magnetron sputtering was expended in this experiment to deposit Cupric Oxide (CuO) onto silicon and quartz substrates.

### **1.2.1 Sputtering Process**

RF magnetron sputtering applies an alternating current in a vacuum environment at radio frequencies between 20 kHz-300GHz, while generating a strong magnetic field near the sputtering target. The alternating current assists in limiting charge accumulation on the target surface and thereby reduces arching and circular erosion. This is accomplished by discharging electrons repeatedly and spreading out the surrounding plasma. The magnetic field traps free electrons to spiral along the magnetic flux above the target surface; allowing for an increased probability of ions to interact and sputter depositing materials with reduced interference. Furthermore, this mechanism confines produced plasma near the target without damaging the deposited film [7].

Acting as a dynamic condition where neutral gas atoms, ions, electrons and photons exist simultaneously in a near balanced state, plasma is generated by ionizing inert sputtering gas, typically Argon (Ar), that is continually pumped into the chamber once the optimal pressure for sputtering is reached. Positively charged ions are generated by

collisions with free electrons and gravitate towards the negatively charged target surface due to the magnets placed directly beneath. Ions ultimately interact with the target surface and the depositing material is ejected and accelerate towards the substrate. In addition, free electrons are also released in the energy transfer and help maintain plasma generation [8].

### **1.3 Chevron CW Laser Annealing**

Chevron CW laser annealing combines several separate techniques to crystallize post-deposition amorphous thin film samples in this experiment. Laser annealing is the process of local irradiation supplied by an energy flux in the form of light, electron flux or plasma flux. Utilizing liquid phase crystallization, a heat source rapidly heats a material and induces an oxidation process underneath the surface, modifying the lattice structure. In addition, the temperature distribution is stimulated to control grain growth direction through the modulation of an energy beam profile. To induce single-crystalline film growth on an amorphous surface, continuous wave (CW) laser annealing (CLA) is used to maximize grain size growth along the scanning direction and is powered either by a diode pumped solid state laser or multi-laser diodes. Normally, a line beam is imposed to achieve controlled crystal orientation, however, a chevron-tipped laser beam is used to address the difficulty in beam modulation and outside lateral growth towards temperature peaks. The chevron tip is achieved when a linear laser diode beam is passed through the central axis of the connected sides of a Dove and cuboid prism. As the laser beam passes through the one sided dove prism

(OSDP) at a tilt angle of  $\theta$ , a part of the laser is flipped upside-down through the Dove prism and the other remains the same through the cuboid prism; causing the linear line beam to bend at an angle of  $2\theta$  [9]. The formation of the chevron tipped laser beam is seen in the schematic diagram in Figure 6.

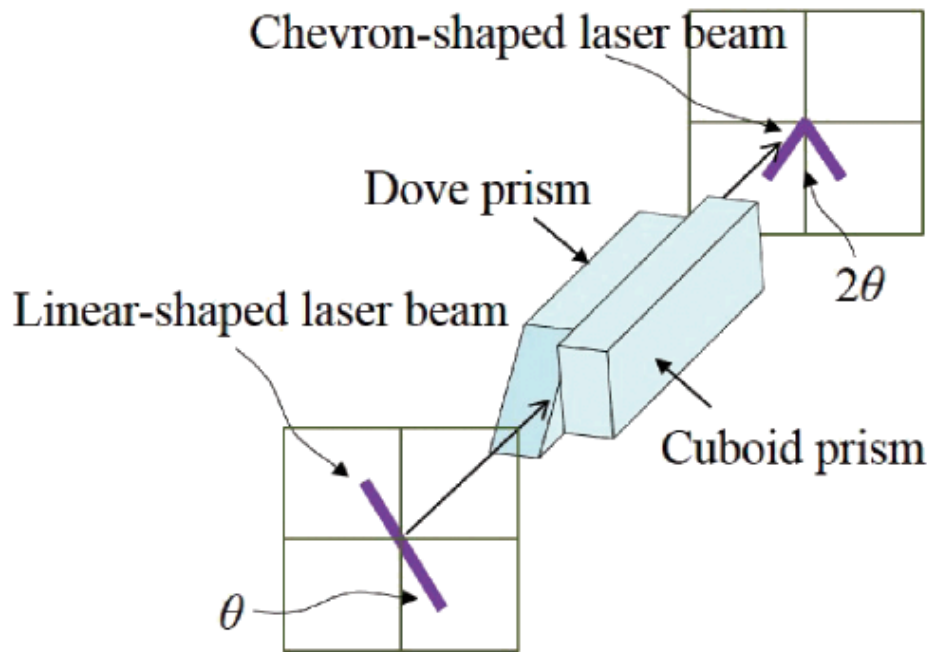


**Figure 6** Schematic Diagram of Chevron Tipped Laser Beam Passing Through the One Sided Dove Prism [9]

To potentially crystallize a given thin film sample, a laser diode is collimated before passing through the one sided Dove prism and focused before the sample. The sample is attached to the side of rotating table, perpendicular to the laser beam and is moved away from the apex of the chevron tip. The beam spot is observed from a microscope

behind the sample and a diagram of the annealing setup is seen in Figure 7, in addition to images of irradiation from a linear and chevron-tipped laser beam, respectively.

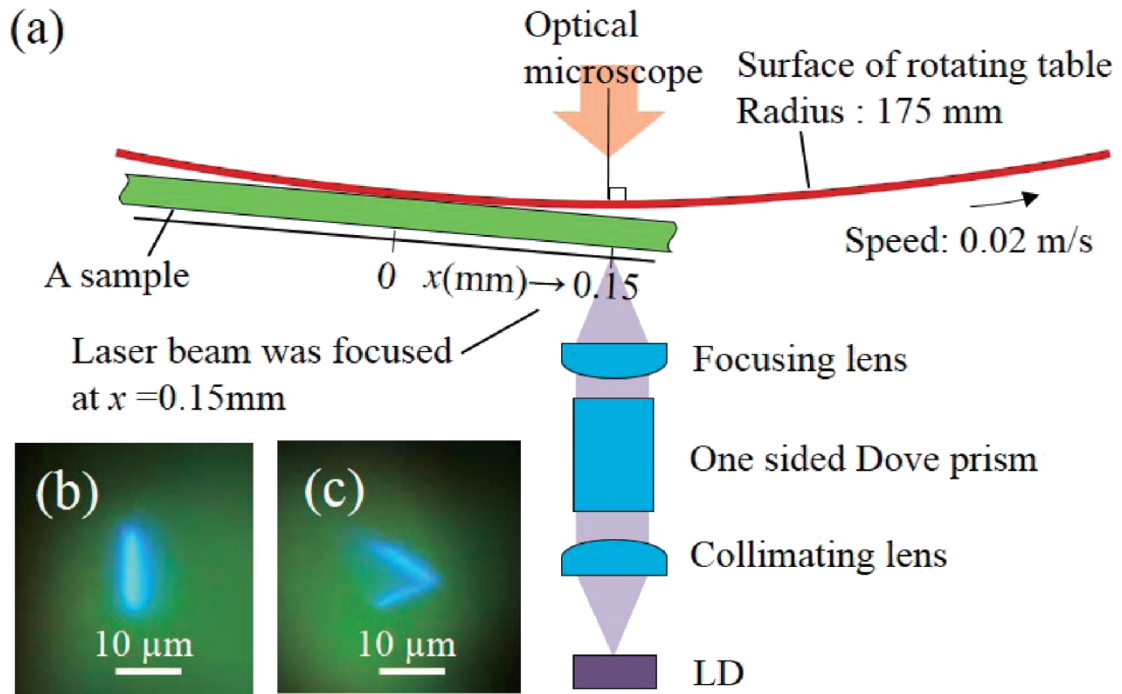


**Figure 7** Sample Diagram of Chevron – Tipped Laser Annealing System and Irradiation Images from Linear (b) and Chevron Tipped Laser Beam [9]

## **II. Procedure**

A total of nine amorphous thin film samples were fabricated with the AJA Orion Sputtering System throughout three separate deposition runs to vary film thicknesses. Each deposition run contained two quartz wafers and two silicon wafers with approximate dimensions of 18mm x 18mm for all samples. This was done in order to maintain consistent deposition conditions for every sample and to avoid any discrepancies within the film growth.

Prior to securing each substrate on the rotating deposition plate, every silicon substrate was cleaned in a separate sonic bath of acetone, isopropyl alcohol, and distilled water for five minutes each. Any remaining liquid present on either side of the substrate was dried with a particle filtered air blower. The quartz substrates were previously cleaned and polished by our collaborator and immediately secured on the deposition plate to avoid any contamination. A CuO sputtering target was used for deposition, however, it is important to note that while it was rated with 99% purity, it was not verified after receiving the targets.

After each deposition run, a quartz and silicon sample were immediately packaged for laser annealing to avoid contamination. The remaining two samples were retained as “witness” samples to be characterized by ellipsometry and atomic force microscopy; these results are seen in the following section.

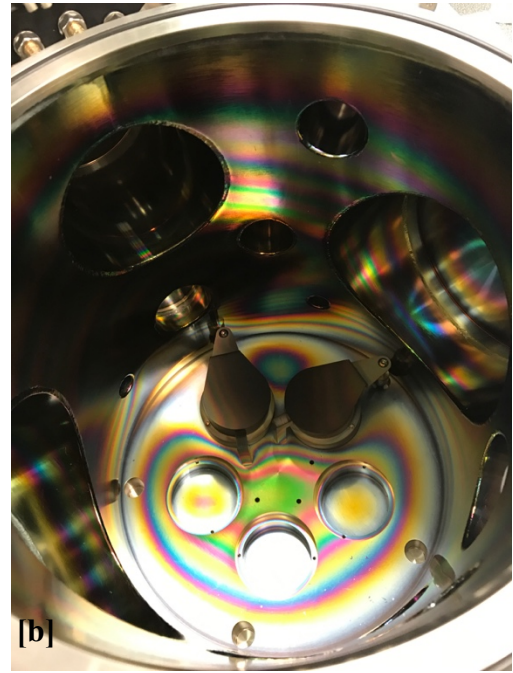
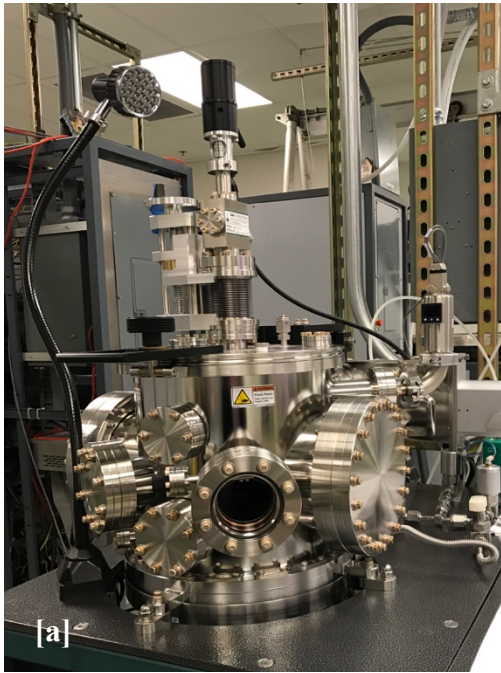


**Figure 8** (a) AJA Sputtering System (b) Covered Sputtering Targets Within Deposition Chamber

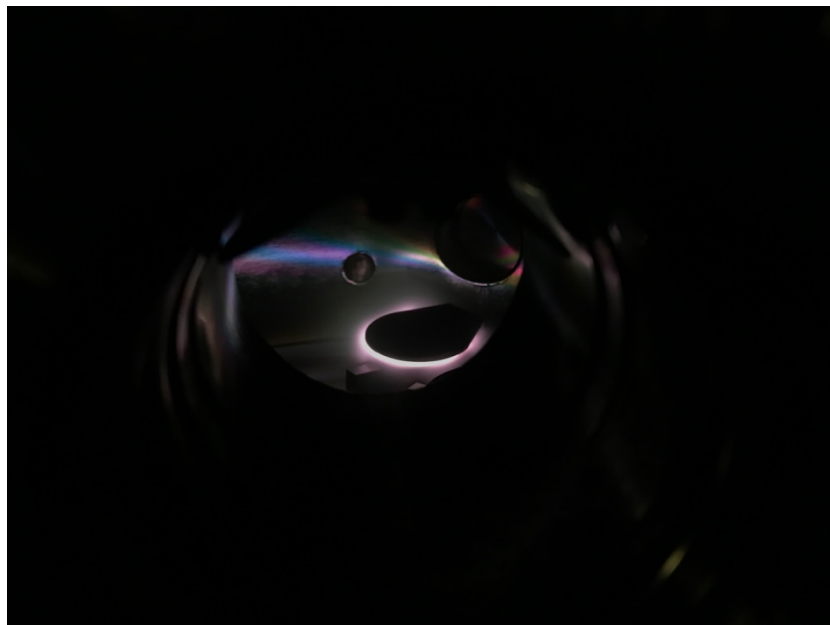


**Figure 9** Ignited Plasma Under Target Shutter

### **III. Results**

To have a variation of film thicknesses, each sample set was deposited at different time lengths and their deposition parameters are noted in Table 1- 3 below. Each sample set was deposited with sputtered CuO in a set Argon gas environment.

Base pressure refers to the pressure required to ignite plasma in the deposition chamber, where the sputtering pressure is when deposition takes place. Forward power refers to the RF power used and correlates to the sputtering rate. Load and Tune values to the amount the capacitor plates are meshed. Forward power, reflected power and voltage values are direct feedback during the experiments.

Deposition Time	3 [mins]	Forward Power	90 [W]
Base Pressure	2.8E-5 [Torr]	Reflected Power	0
Sputtering Pressure	1.5E-2 [Torr]	Voltage	-140 [V]
Load/Tune	18%/85%	Argon Flow	14 [sccm]

**Table 1** Sample A Deposition Parameters

Deposition Time	10 [mins]	Forward Power	90 [W]
Base Pressure	2.7E-5 [Torr]	Reflected Power	0
Sputtering Pressure	1.1E-2 [Torr]	Voltage	-124 [V]
Load/Tune	28%/79%	Argon Flow	14 [sccm]

**Table 2** Sample B Deposition Parameters

Deposition Time	40 [mins]	Forward Power	90 [W]
Base Pressure	2.6E-5 [Torr]	Reflected Power	0
Sputtering Pressure	1.18E-2 [Torr]	Voltage	-149 [V]
Load/Tune	29%/79%	Argon Flow	14 [sccm]

**Table 3** Sample C Deposition Parameters

### 3.1 Post Deposition Characterization

#### Ellipsometry

Ellipsometry measures the change in polarization as light reflects or transmits from a material. Specifically, it measures the change of polarized light upon reflection or transmission of the p-plane and s-plane<sup>1</sup>. This polarization change is calculated by the amplitude ratio,  $\Psi$ , and the phase difference,  $\Delta$ . To determine the amount of growth, post-deposition samples are studied for their film thickness and optical properties, specifically, their refractive index (n) and extinction coefficient values (k).

Film thickness is determined by the interference between light both reflecting from the sample surface and traveling through the film. The constructive/destructive interference is dependent on the relative phase of the rejoining light. The portion of light that travels through the entire film must return to the surface in order to have a comprehensive measurement.

---

<sup>1</sup> p-plane is parallel to the incident plane where s-plane is perpendicular

The refractive index describes how quickly light, at a certain wavelength, travels through a material, specifically, the phase velocity compared to the speed of light. Similarly, the extinction coefficient describes the loss of wave energy or light intensity to the material. When related to amorphous thin film materials,  $n$  and  $k$  are described through the Forouhi-Bloomer dispersion equations with full dependence on photon energy,  $E$ , through five model parameters [10].

$$n(E) = n(\infty) + \frac{(B_0E + C_0)}{E^2 - BE + C}$$

$$k(E) = \frac{A(E - E_g)^2}{E^2 - BE + C}$$

Where  $E_g$  corresponds to the material optical band gap energy;  $A$ ,  $B$ ,  $C$  are positive constants dependent on material band structure and  $n(\infty)$  is the refractive index at  $E = \infty$ . Parameters,  $B_0$  and  $C_0$  are described as

$$B_0 = \frac{A}{Q} \left( \frac{-B^2}{2} + E_g B - E_g^2 + C \right)$$

$$C_0 = \frac{A}{Q} \left[ (E_g^2 + C) \frac{B}{2} - 2E_g C \right]$$

$$Q = \frac{1}{2} (4C - B^2)^{1/2}$$

Post-deposition samples were measured for film thickness, optical constants, film roughness. n-k values were found over a range of wavelengths and through set model parameters. For each sample, three separate measurements were made at three different spots of the sample to ensure a comprehensive measurement of the entire thin film and averaged. RMSE values are included to validate the accuracy of each measurement. Table 4 lists the film thickness, roughness and RMSE where Table 5 lists the n-k values for each measurement at 405nm and 632nm of Sample A. This is duplicated for Sample B and C in Tables 6 – 9 in respective measurements. 405nm was chosen as the wavelength used in chevron cw laser annealing and 632nm is the standard wavelength of measurement.

For the following data graphs, both stimulated and measured reflection (%Rs), psi ( $\Psi$ ) and Delta ( $\Delta$ ) values are plotted. All stimulated measurements are calculated by initial model parameters after calibration. It is important to note that the reflection is the reflection of the sample at  $0^\circ$ . Ideally, the maxima of the measured reflection curve at  $0^\circ$  will match with the simulated reflection curve that is calculated without the film thickness for a single layer sample. Therefore, thicker films may exhibit partial incoherence that will suppress the reflection intensity.

### Sample A

	[1]	[2]	[3]	[average]
Thickness [nm]	3.92	3.70	3.90	3.84
Roughness [nm]	1.16	0.01	0.11	0.43
RMSE	0.71	0.70	0.66	0.69

**Table 4** Sample A - Film Thickness, Roughness and RMSE Values

As expected, a smooth thin film was grown with an averaged thickness of 3.84 nm and averaged roughness of 0.43nm for Sample A. The averaged sputtering rate is 1.28 [nm/min].

405nm	[1]	[2]	[3]	[average]
n	3.05	2.50	2.66	2.74
k	1.19	0.97	0.09	0.75
632nm				
n	2.04	2.76	2.94	2.58
k	0.13	0.03	0	0.05

**Table 5** Sample A - Refractive Index and Extinction Coefficient Values

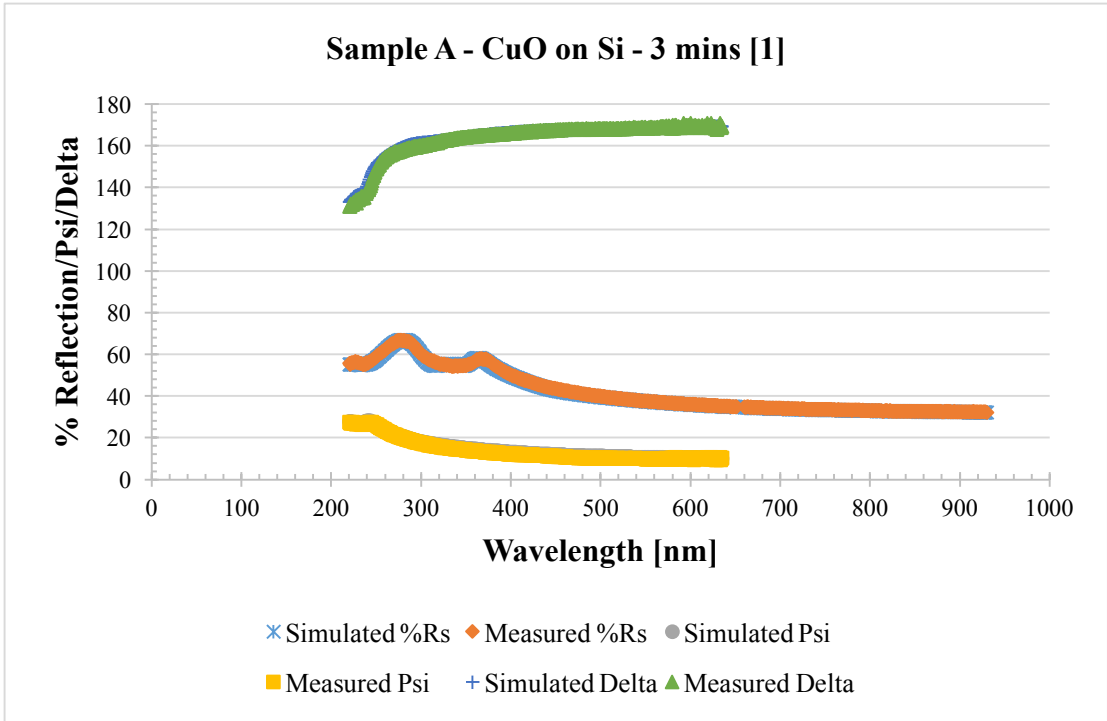


**Figure 10** Sample A- Measurement 1 - Reflection/Psi/Delta Values

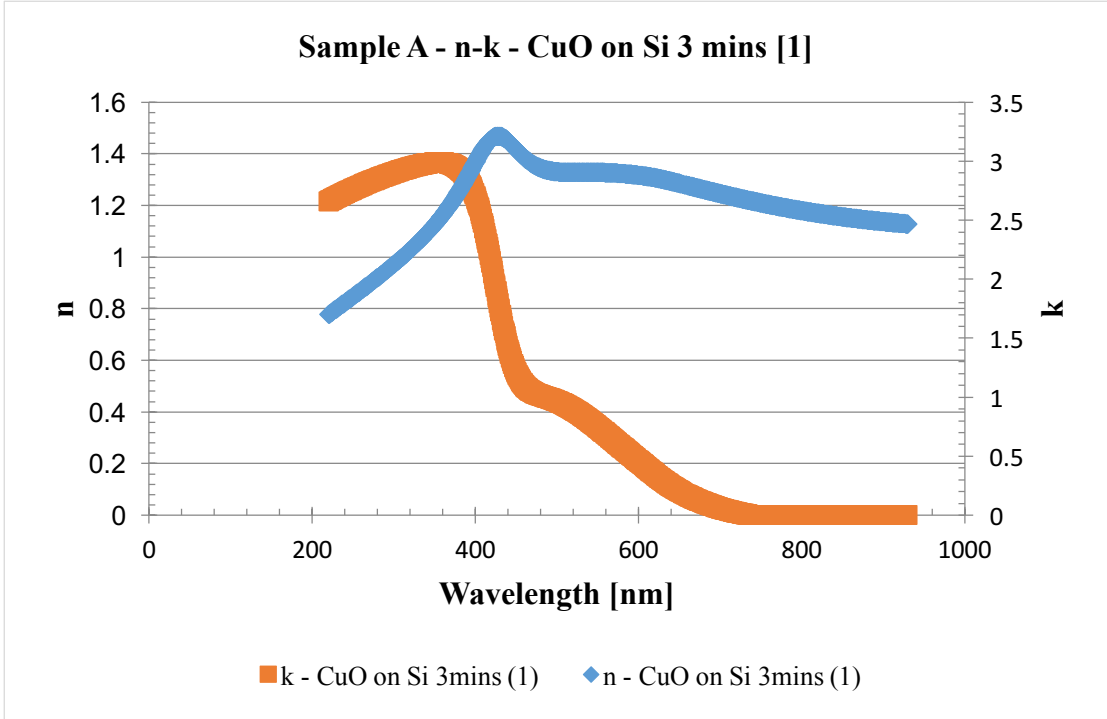


**Figure 11** Sample A – Measurement 1 - n-k values

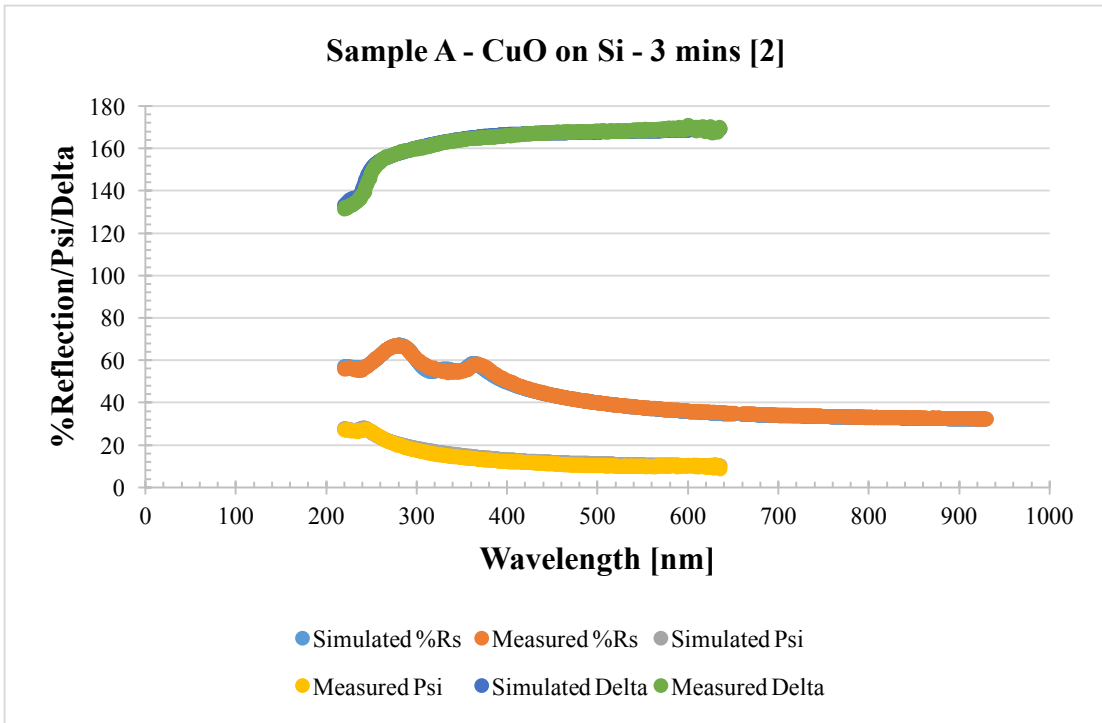


**Figure 12** Sample A – Measurement 2 - Reflection/Psi/Delta Values

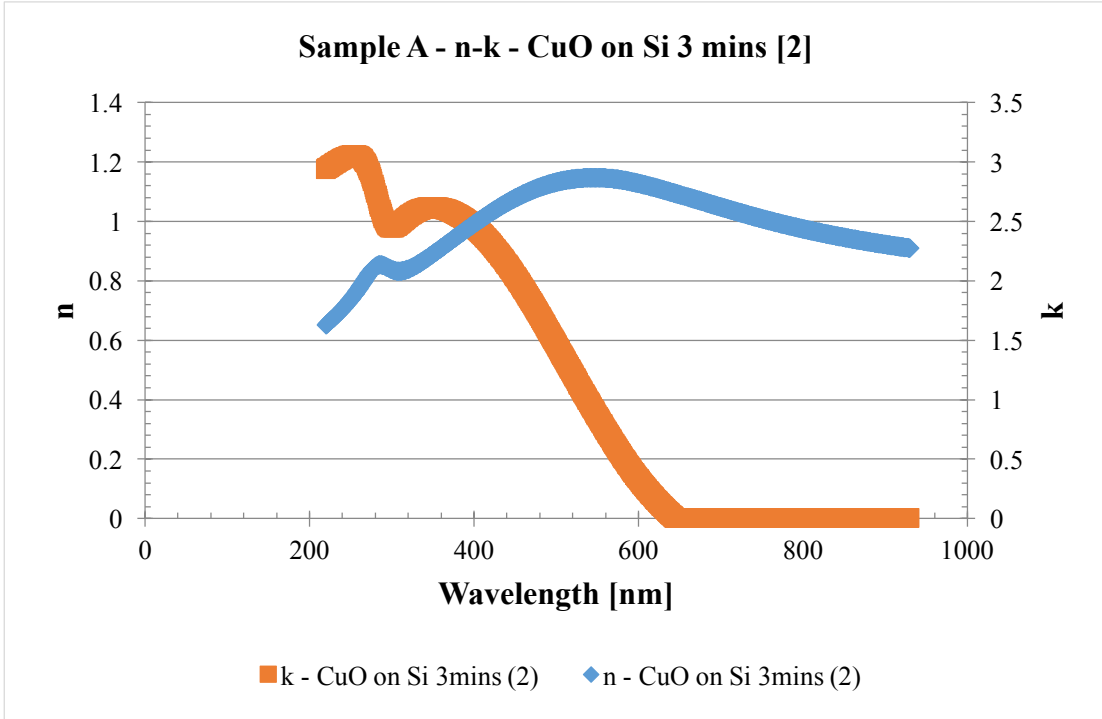


**Figure 13** Sample A – Measurement 2 - n-k values

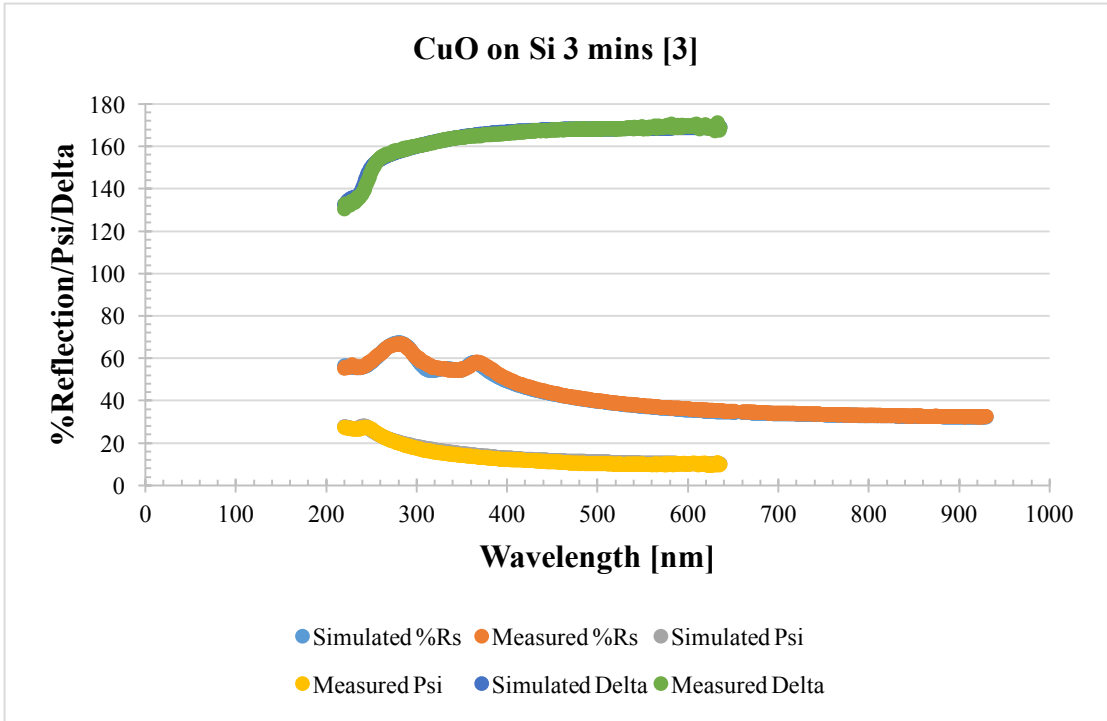


**Figure 14** Sample A – Measurement 3 - Reflection/Psi/Delta Values

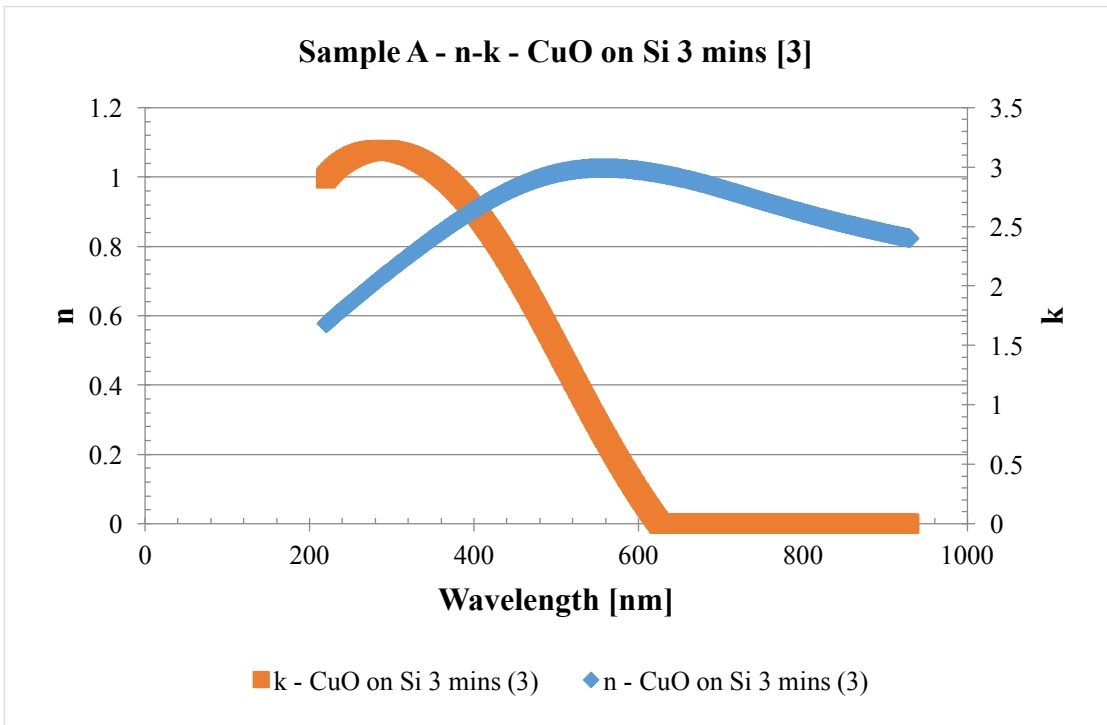


**Figure 15** Sample A – Measurement 3 - n-k values

**Sample B**

	[1]	[2]	[3]	[average]
Thickness [nm]	15.4	15.24	15.82	15.49
Roughness [nm]	0.33	0.72	0.47	0.51
RMSE	0.77	0.83	0.74	0.78

**Table 6** Sample B – Film Thickness, Roughness and RMSE Values

405nm	[1]	[2]	[3]	[average]
n	2.06	1.95	2.10	2.04
k	0.66	0.46	0.75	0.62
632nm				
n	2.24	2.07	2.31	2.21
k	0.29	0.27	0.30	0.29

**Table 7** Sample B – Refractive Index and Extinction Coefficient Values

The averaged sputtering rate for Sample B was calculated to be 1.549 [nm/min].

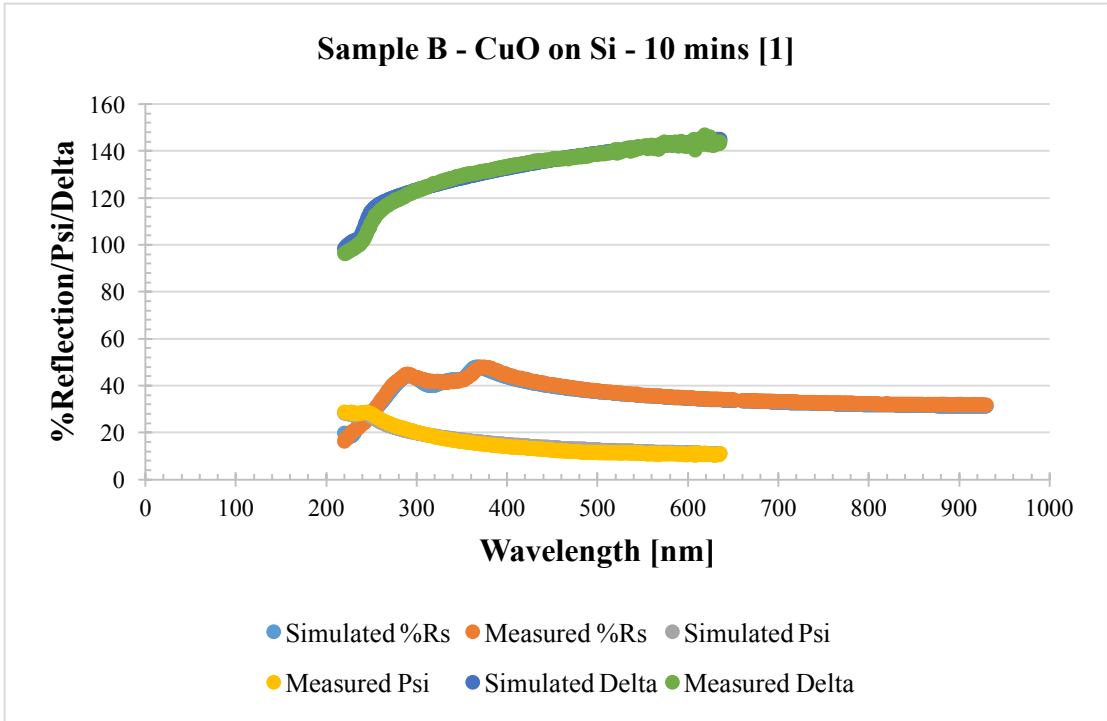


**Figure 16** Sample B – Measurement 1 - Reflection/Psi/Delta Values

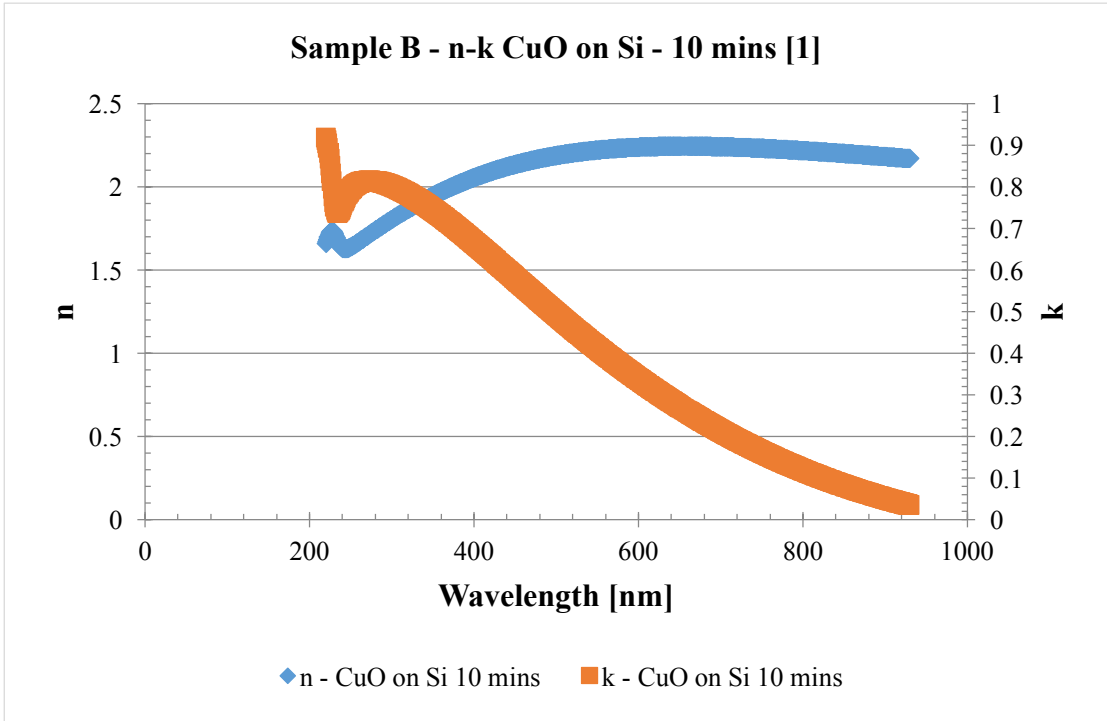


**Figure 17** Sample B – Measurement 1 - n-k values

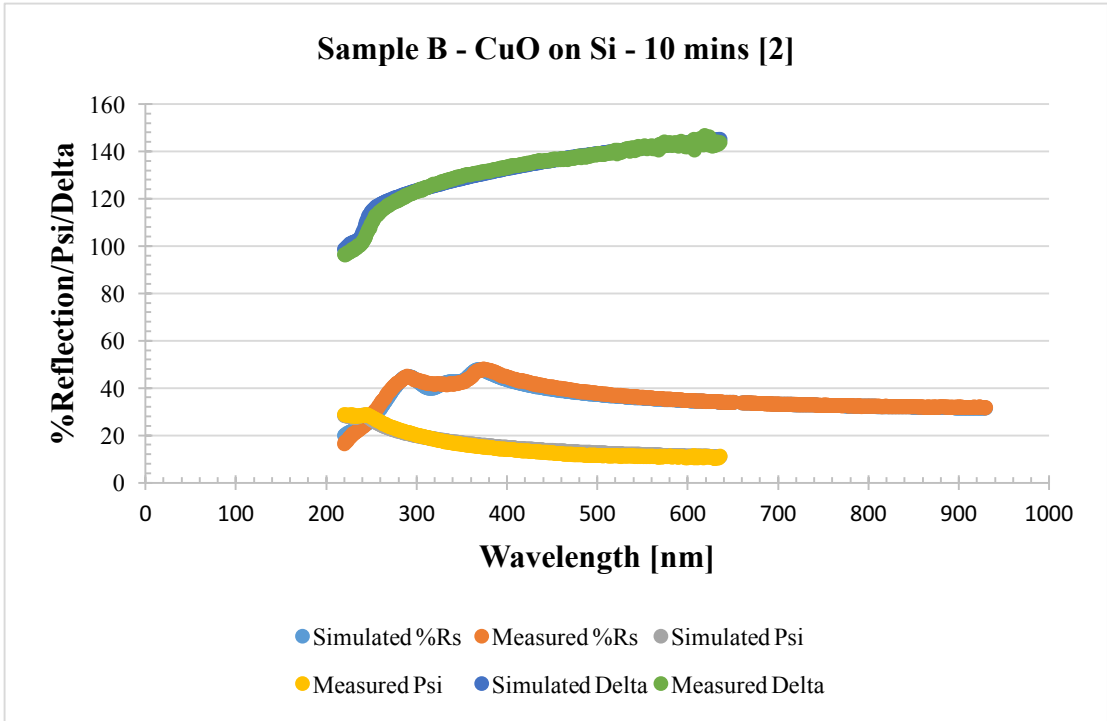


**Figure 18** Sample B – Measurement 2 - Reflection/Psi/Delta Values

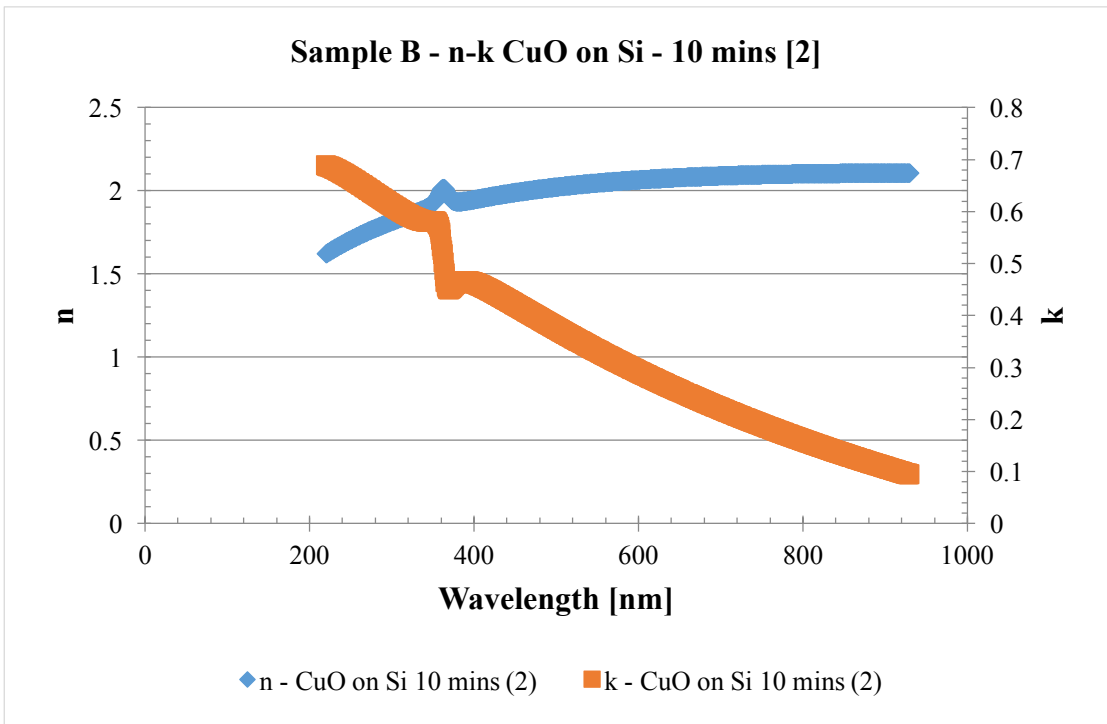


**Figure 19** Sample B – Measurement 2 – n-k values

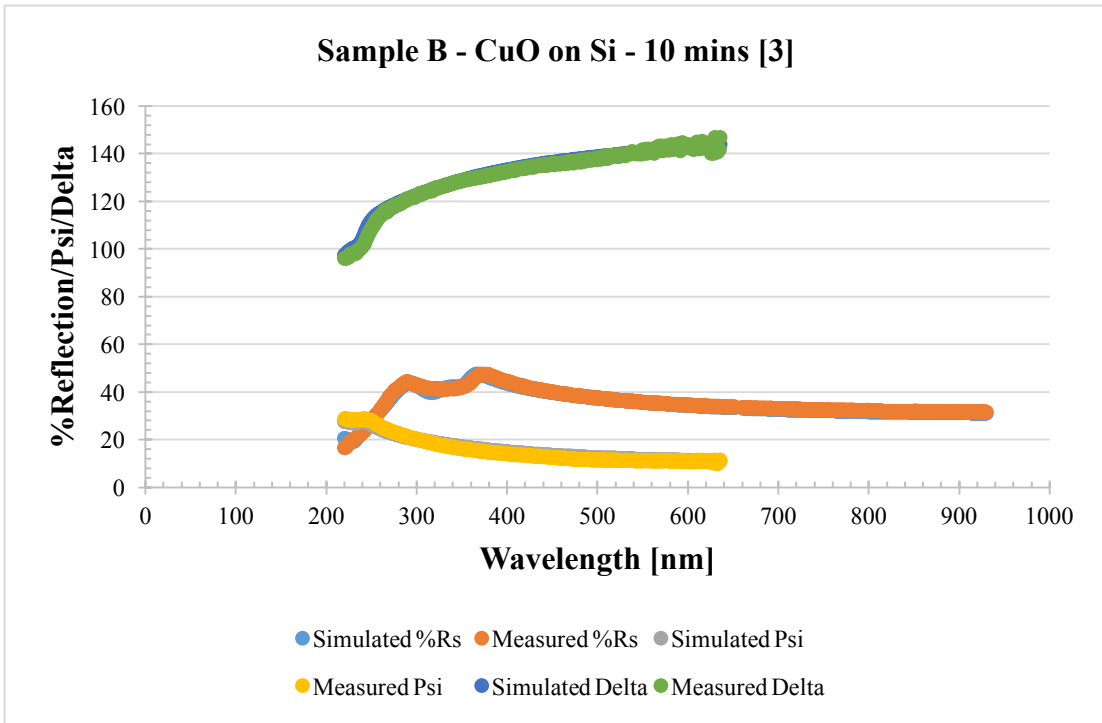


**Figure 20** Sample B – Measurement 3 - Reflection/Psi/Delta Values

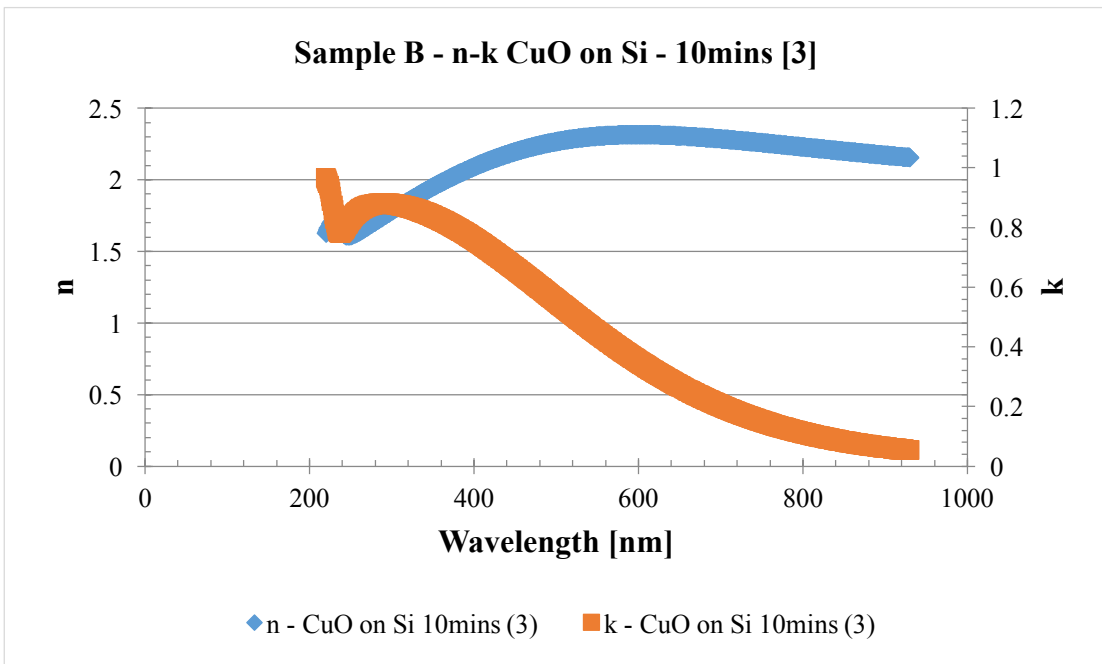


**Figure 21** Sample B – Measurement 3 – n-k values

**Sample C**

	[1]	[2]	[3]	[average]
Thickness [nm]	97.44	98.86	98.27	98.19
Roughness [nm]	2.42	2.24	8.7	4.45
RMSE	0.92	0.91	0.91	0.91

**Table 8** Sample C – Film Thickness, Roughness and RMSE Values

405nm	[1]	[2]	[3]	[average]
n	1.61	1.61	1.62	1.61
k	0.47	0.47	0.46	0.47
632nm				
n	1.58	1.57	1.50	1.55
k	0.35	0.33	0.32	0.33

**Table 9** Sample C – Refractive Index and Extinction Coefficient

The averaged sputtering rate was calculated to be 2.45 [nm/min].

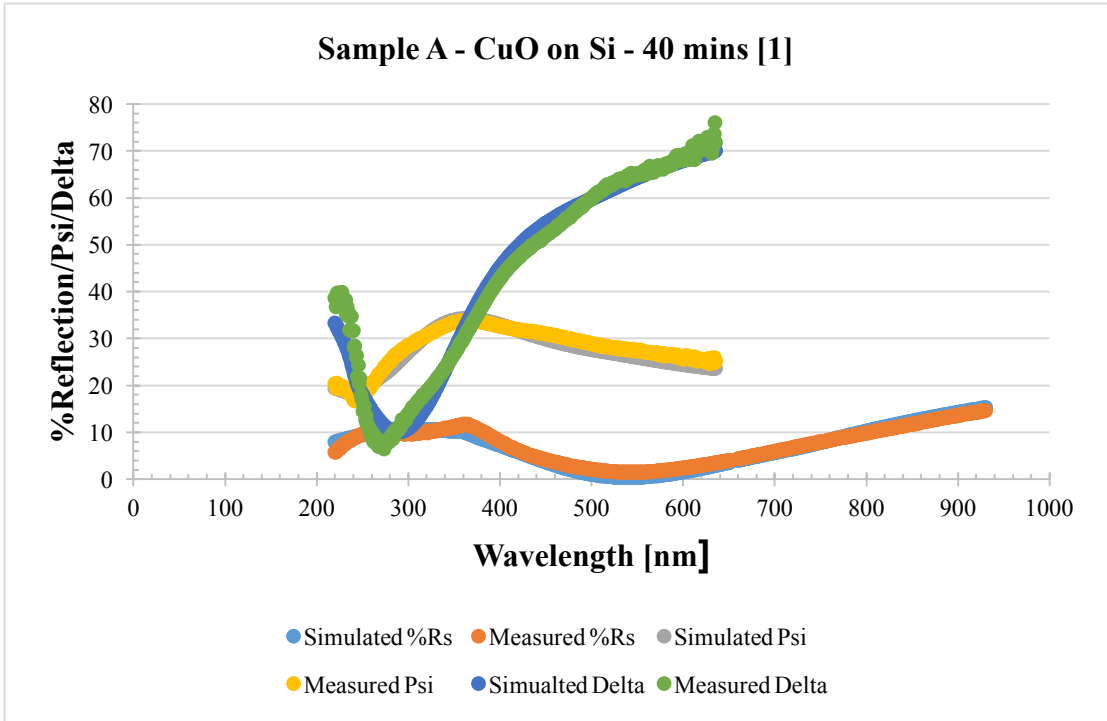


**Figure 22** Sample C – Measurement 1 - Reflection/Psi/Delta Values

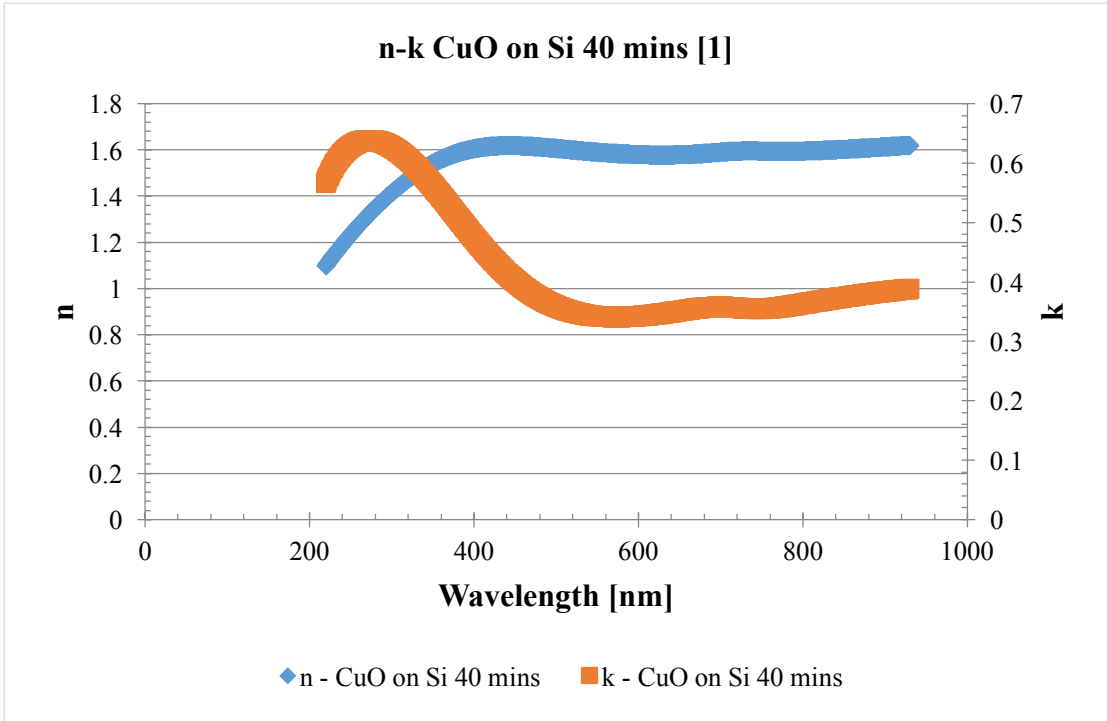


**Figure 23** Sample C – Measurement 1 – n-k values

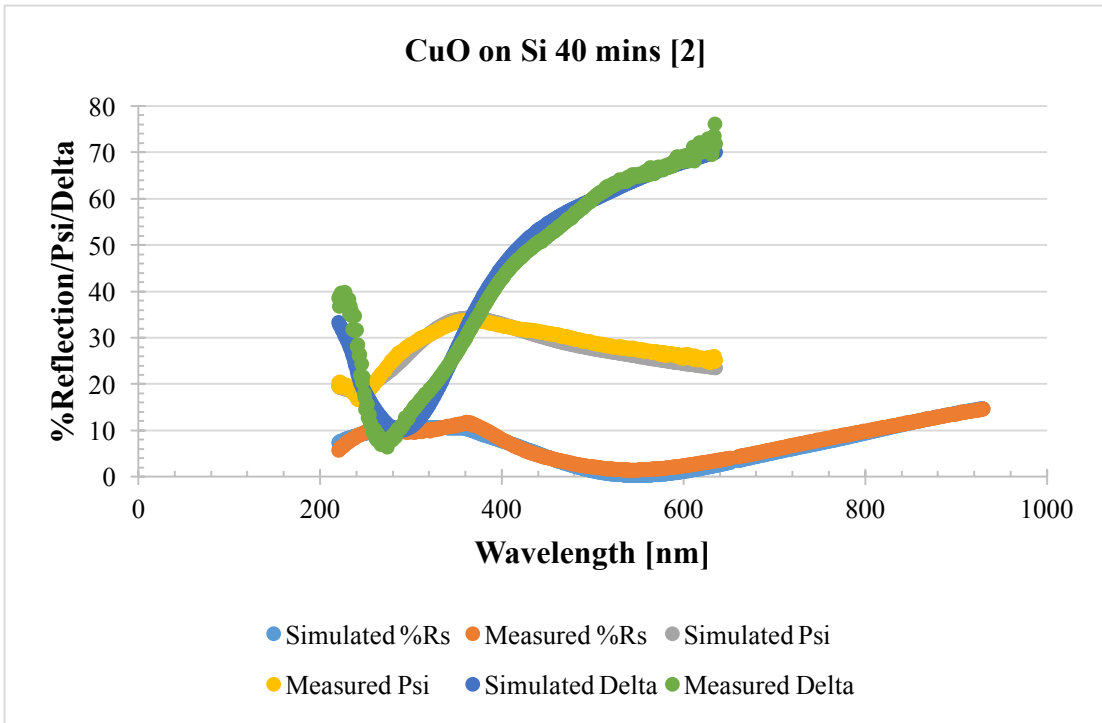


**Figure 24** Sample C – Measurement 2 - Reflection/Psi/Delta Values

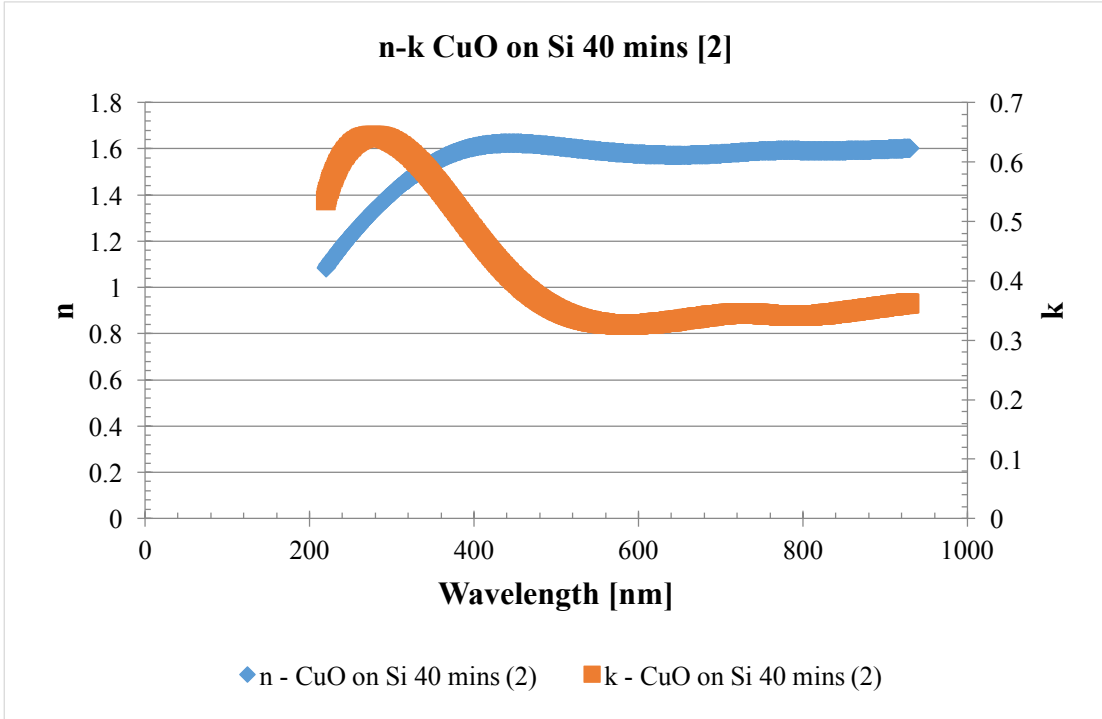


**Figure 25** Sample C – Measurement 2 – n-k values

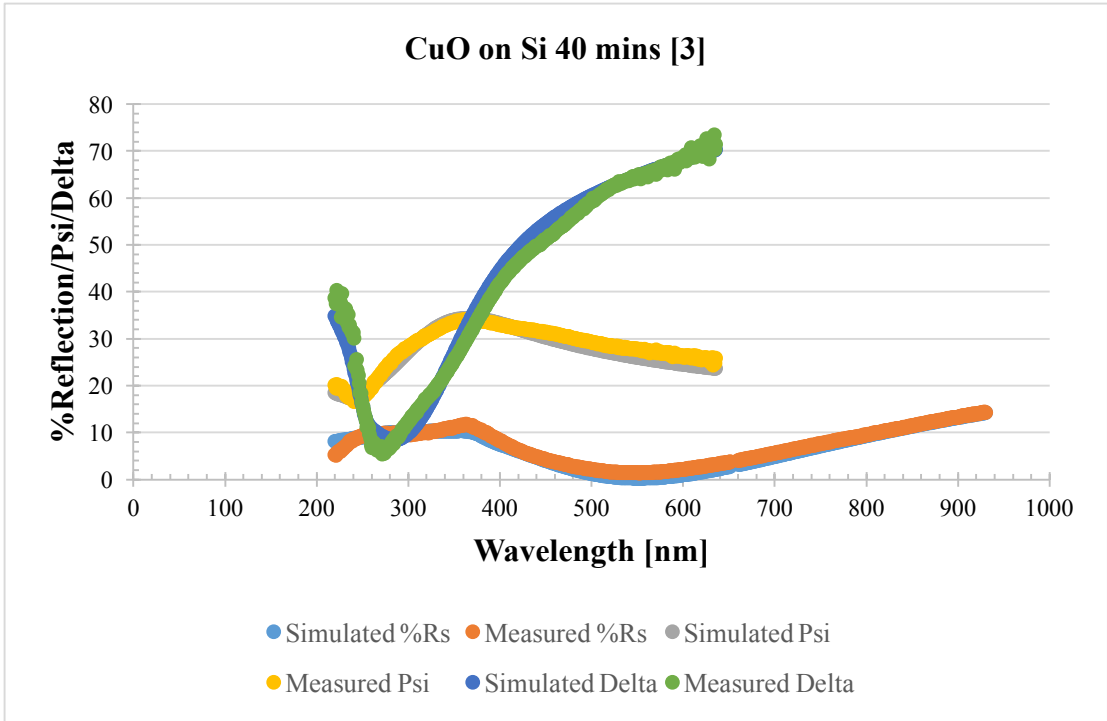
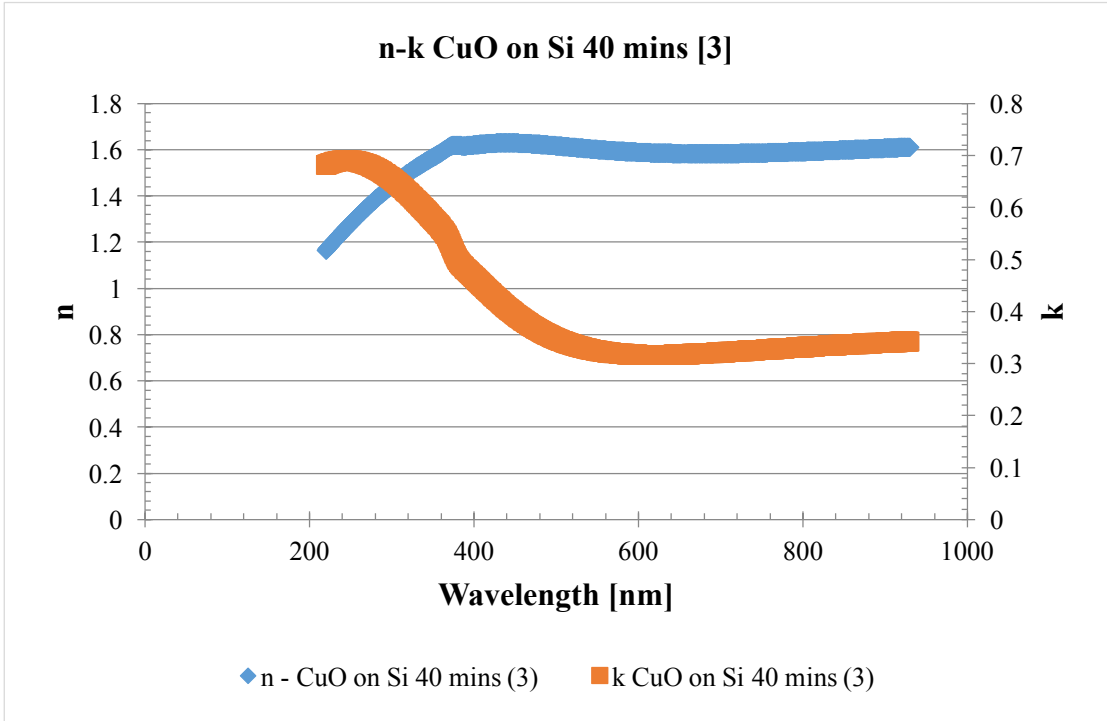


**Figure 26** Sample C – Measurement 3 - Reflection/Psi/Delta Values



Throughout Figures 10 – 26, the plotted simulated and measured data for reflection, psi and delta values are fairly similar and indicate the accuracy of the input model parameters used. However, there is a noticeable difference in Sample C, Figures 22, 24, 26. When compared to Sample A and B, the data in Sample C doesn't align as smoothly. This most likely due to the increased model parameters used for Sample C due to the increased thickness. In addition, the extinction coefficient peaks consistently around a wavelength of 300nm, indicating that the film mostly absorbs entering light before the 405nm wavelength of the chevron cw laser. This is also seen in Figure 15 for Sample B, but is not as distinct as seen across all measurements in Sample C. This is particularly important in indicating the likelihood of post – annealing crystallization of the thin films. However, it is important to note a slight inaccuracy in measurements. Specifically seen in the refractive index plot of Sample A in Figures 11 and 13, there is a slight “notch” around 400nm. This similar inconsistency is also seen in the extinction coefficient plots for Sample B in Figure 17, 19, and 21. A continued analysis of ellipsometry results are compiled and compared with AFM results below.

### **Atomic Force Microscopy (AFM)**

Atomic force microscopy (AFM) is an imaging technique used for surface measurement by “rastering” the material surface with a small probe. The probe tip is attached to a cantilever where a laser beam is directed and reflected to a split diode photo-detector. As the cantilever oscillates laterally, the position of the laser on the photo-detector changes, creating top and bottom photocurrents on respective diodes. The difference in these photocurrents indicates how much the cantilever bends as it scans the sample surface. Designed to measure local properties of height, friction and magnetism, AFM utilizes Hooke’s law and the restoring force is calculated by measuring the deflection of the cantilever [11].

All post deposition measurements were made in “constant contact” mode, where the probe tip touches the same surface at all times. This mode directly measures the probe’s position with respect to the cantilever deflection.

Additional measurements of RMS roughness, mean roughness, peak height and pit depth were recorded at 1 $\mu$ m and 10 $\mu$ m scan sizes with 512 and 1024 resolutions, respectively, for all samples, including a ‘bare’ quartz sample, in Tables 10 – 13. The bare quartz sample contains no deposited material and serves as a reference sample. Each sample at its respective scan size and resolution was measured in three different locations across the sample and averaged for comparison. The RMS thickness and roughness measurements are used to compare to ellipsometry measurements for accuracy.

**Bare Quartz Sample**

	[a]	[b]	[c]	[avg]
RMS Roughness [nm]	0.6125	0.5131	0.7502	0.6253
Mean Roughness [nm]	0.4466	0.3914	0.5818	0.4733
Peak Height [nm]	2.023	2.861	2.687	2.524
Pit Depth [nm]	6.094	3.634	4.739	4.822

**Table 10** Bare Quartz Reference

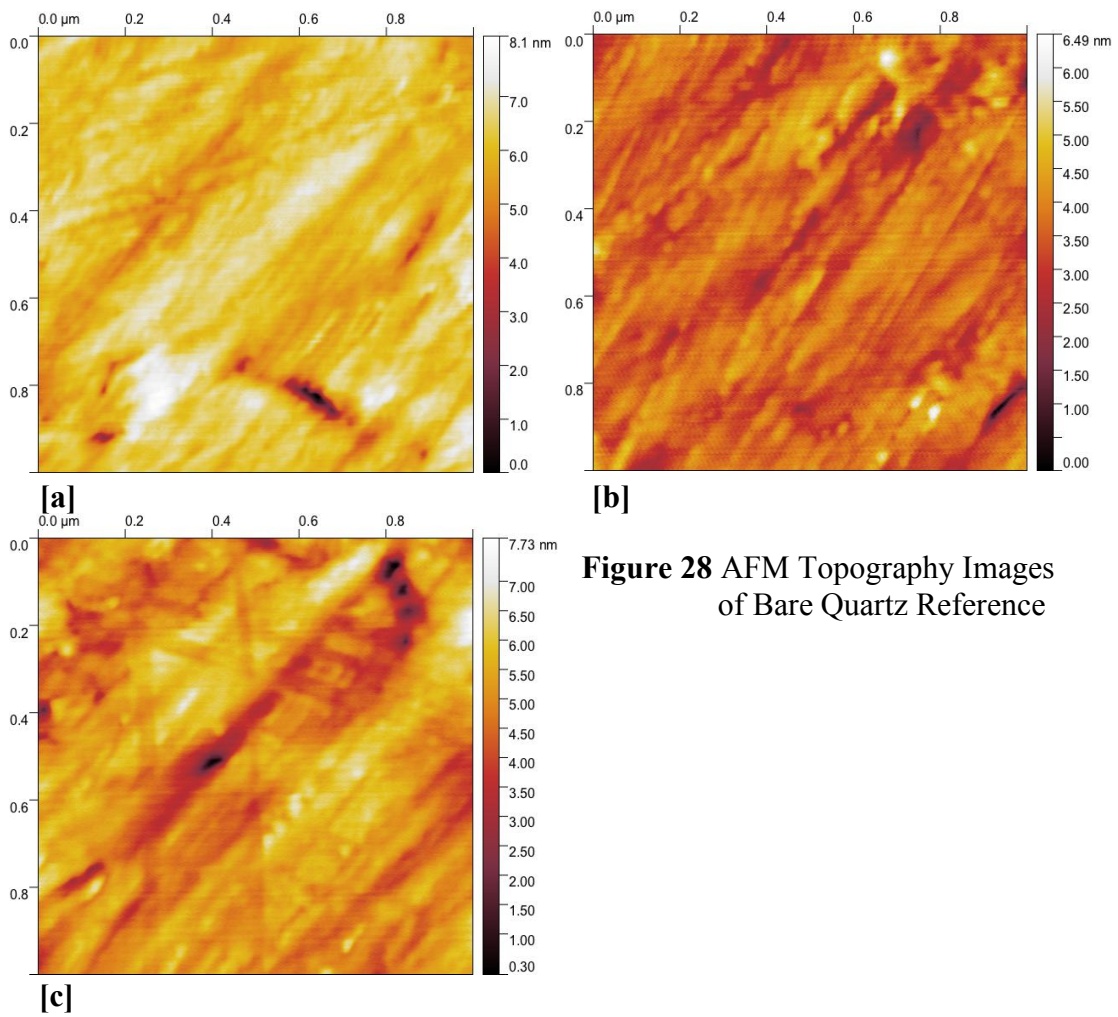


**Figure 28** AFM Topography Images of Bare Quartz Reference

**Sample A - 1 $\mu$ m**

	[a]	[b]	[c]	[avg]
RMS Roughness [nm]	0.5858	0.5341	0.8185	0.6461
Mean Roughness [nm]	0.4476	0.4211	0.5511	0.4733
Peak Height [nm]	4.085	2.724	8.66	5.156
Pit Depth [nm]	4.44	4.597	4.38	74.80

**Table 11** Sample A 1 $\mu$ m

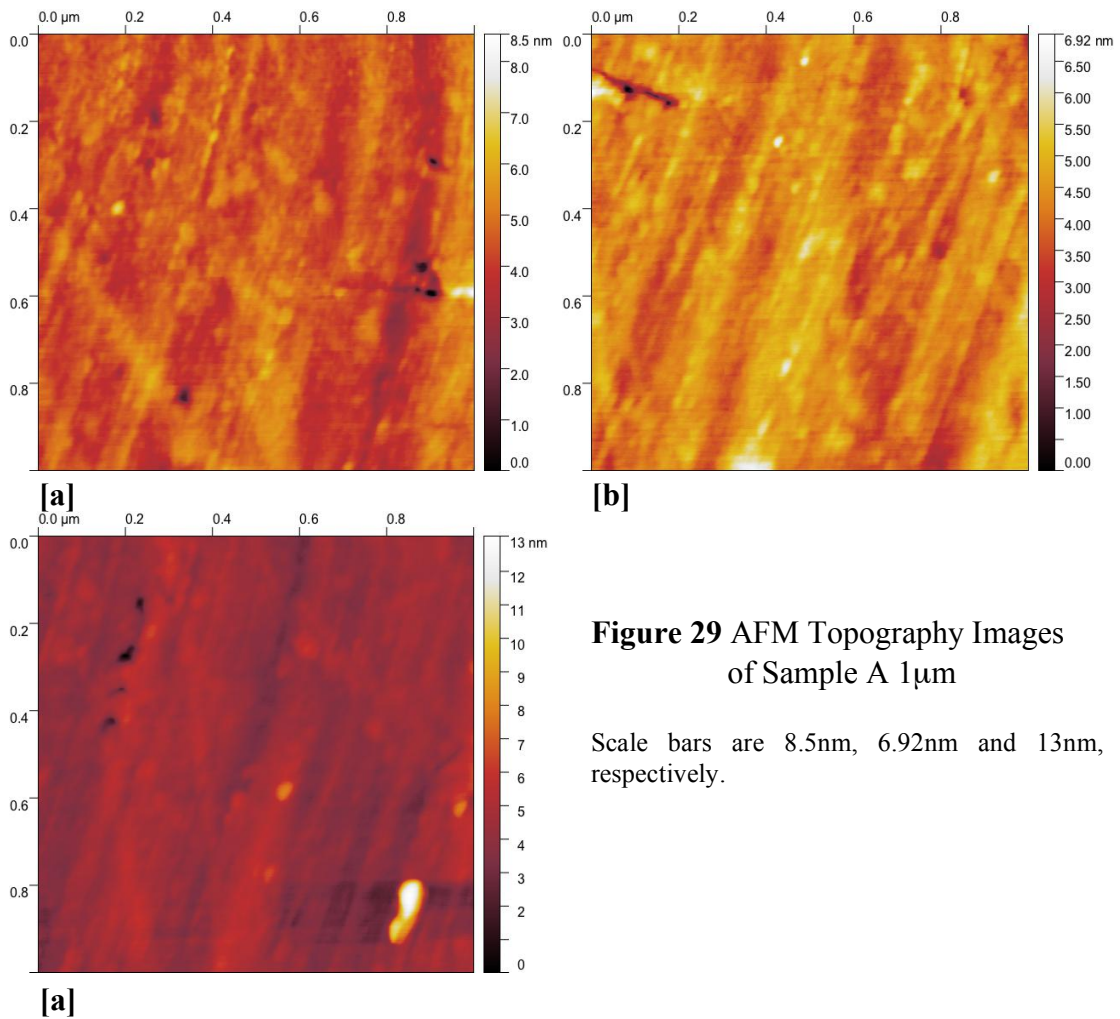


**Figure 29** AFM Topography Images of Sample A 1 $\mu$ m

Scale bars are 8.5nm, 6.92nm and 13nm, respectively.

**Sample A - 10 $\mu$ m**

	[a]	[b]	[c]	[avg]
RMS Roughness [nm]	0.5473	0.5031	0.5346	0.5283
Mean Roughness [nm]	0.4052	0.3826	0.3914	0.3931
Peak Height [ $\mu$ m]	9.95	6.028	8.63	8.203
Pit Depth [nm]	2.2	2.331	1.88	2.137

**Table 12** Sample A 10 $\mu$ m

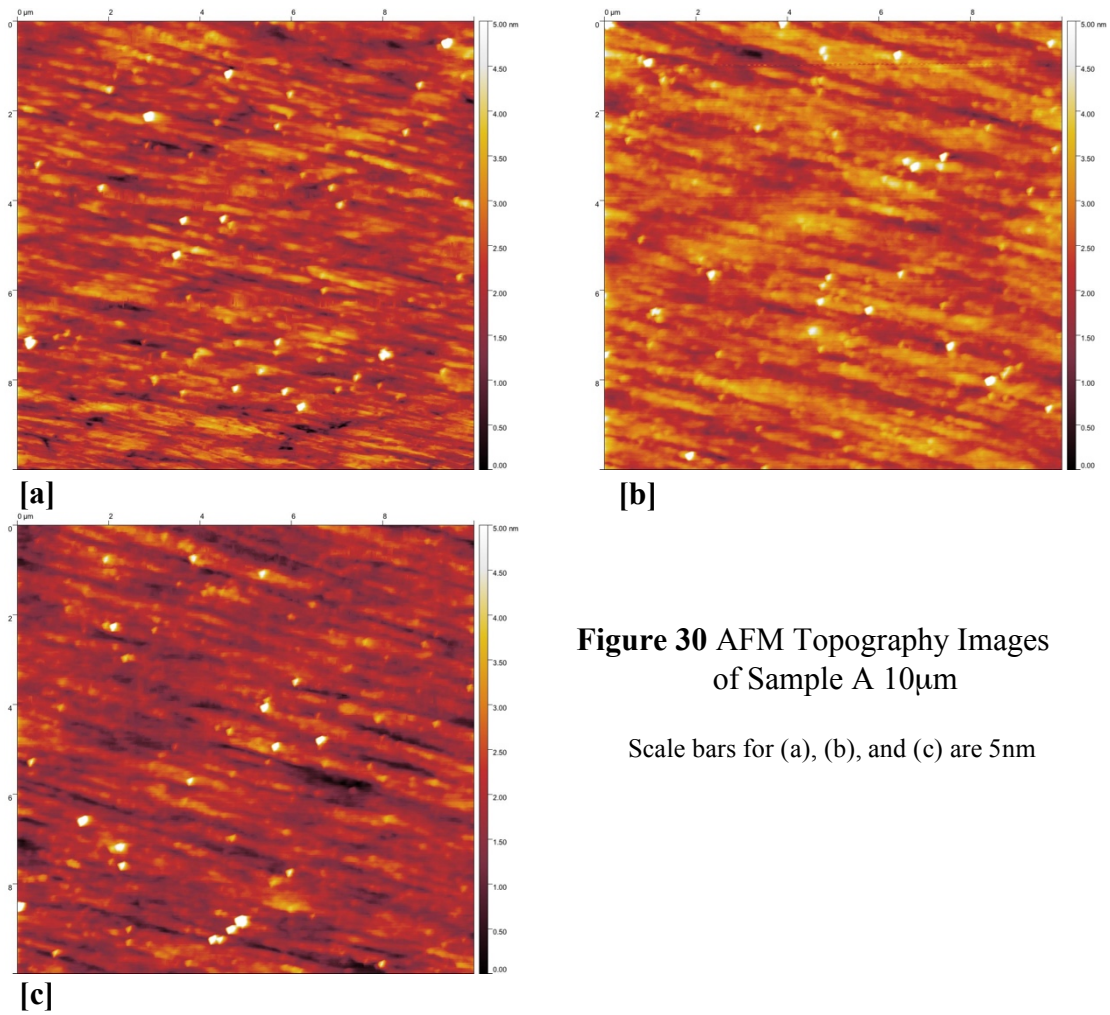


**Figure 30** AFM Topography Images of Sample A 10 $\mu$ m

Scale bars for (a), (b), and (c) are 5nm

**Sample B - 1 $\mu$ m**

	[a]	[b]	[c]	[avg]
RMS Roughness [nm]	0.5979	0.6873	0.4936	0.5929
Mean Roughness [nm]	0.4737	0.544	0.3929	0.4702
Peak Height [nm]	3.2	2.847	1.915	2.654
Pit Depth [nm]	3.455	2.588	1.859	2.634

**Table 13** Sample B 1 $\mu$ m

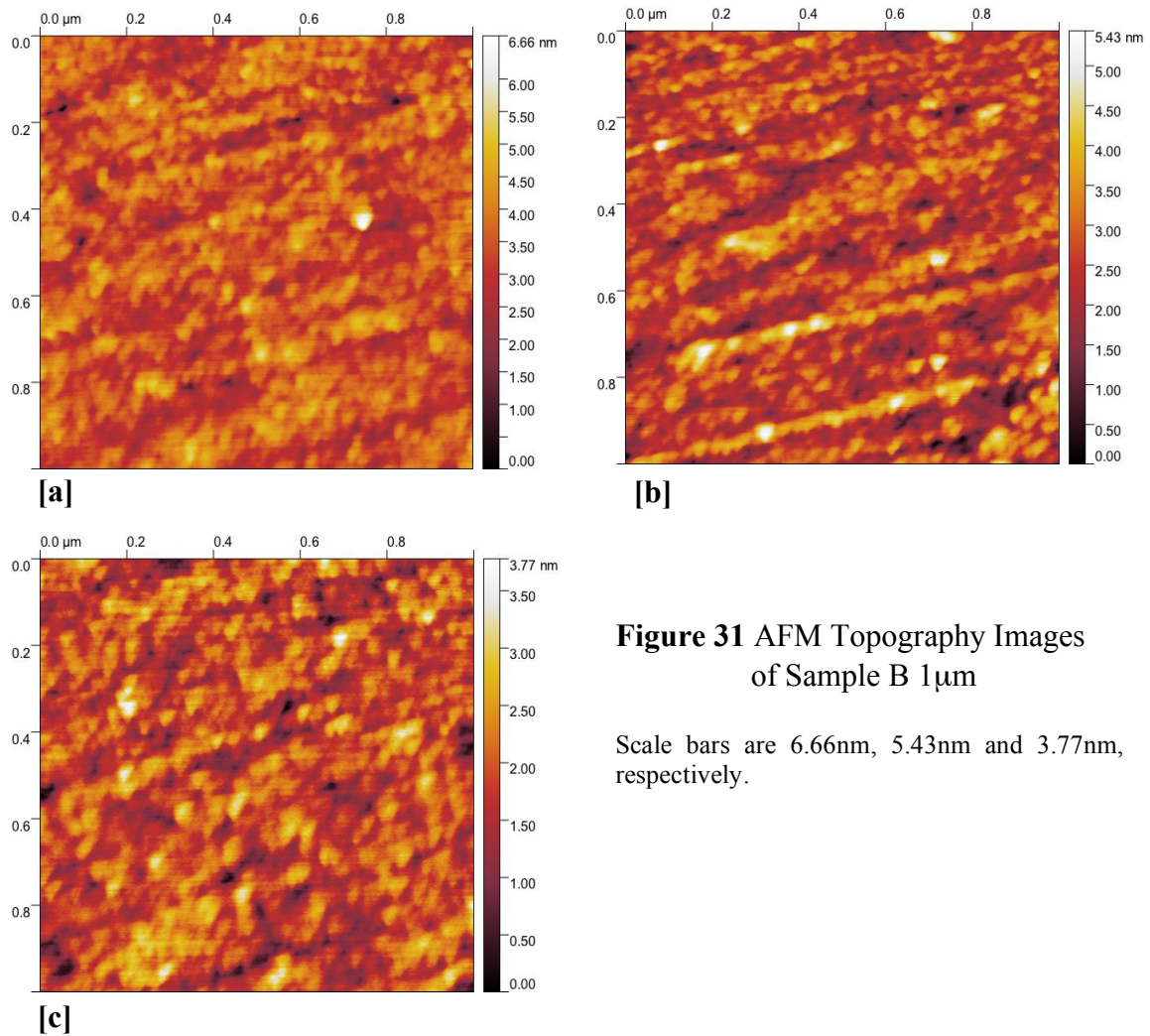


**Figure 31** AFM Topography Images of Sample B 1 $\mu$ m

Scale bars are 6.66nm, 5.43nm and 3.77nm, respectively.

**Sample B - 10 $\mu$ m**

	[a]	[b]	[c]	[avg]
RMS Roughness [nm]	0.757	0.5718	0.6783	0.6690
Mean Roughness [nm]	0.5072	0.4481	0.4805	0.4786
Peak Height [nm]	25.9	7.433	13.96	15.76
Pit Depth [nm]	2.61	2.034	2.57	2.405

**Table 14** Sample B 10 $\mu$ m

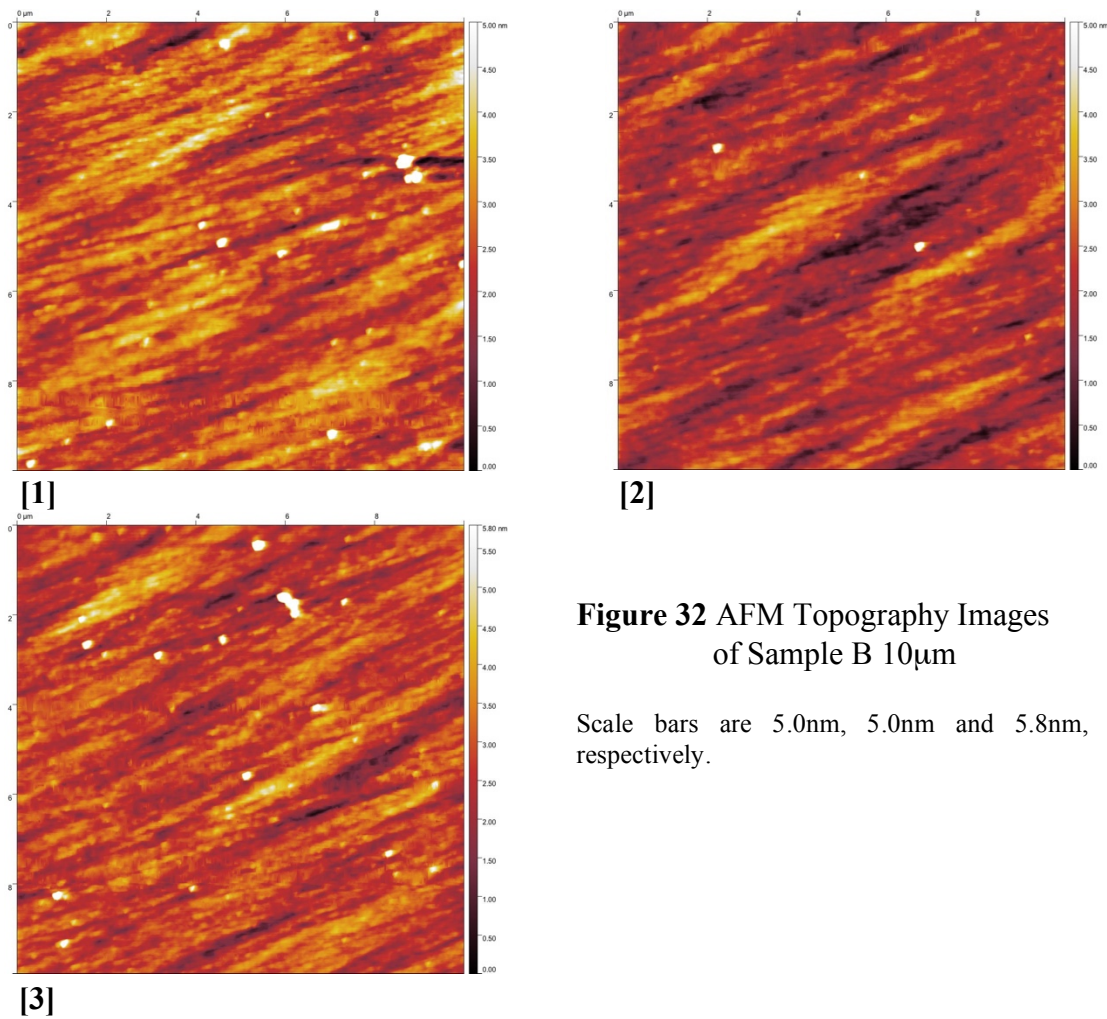


**Figure 32** AFM Topography Images of Sample B 10 $\mu$ m

Scale bars are 5.0nm, 5.0nm and 5.8nm, respectively.

**Sample C - 1 $\mu$ m**

	[a]	[b]	[c]	[avg]
RMS Roughness [nm]	1.755	1.526	1.42	1.567
Mean Roughness [nm]	1.383	1.211	1.118	1.237
Peak Height [nm]	6.38	5.42	5.4	5.733
Pit Depth [nm]	8.79	6.77	6.14	7.233

**Table 15** Sample C 1 $\mu$ m

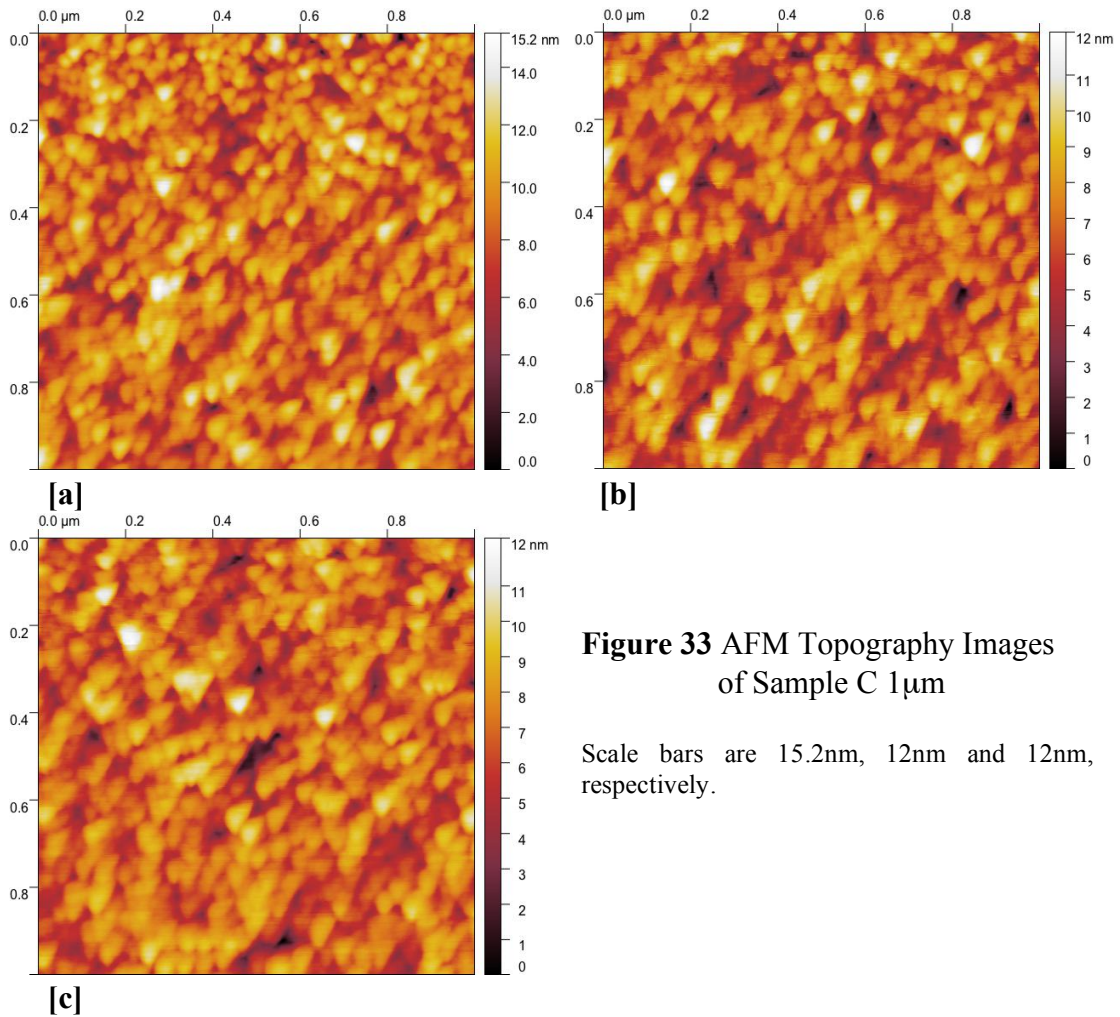


**Figure 33** AFM Topography Images of Sample C 1 $\mu$ m

Scale bars are 15.2nm, 12nm and 12nm, respectively.

**Sample C - 10 $\mu$ m**

	[a]	[b]	[c]	[avg]
RMS Roughness [nm]	0.8365	0.751	0.9483	0.8453
Mean Roughness [nm]	0.6381	0.6012	0.7075	0.6489
Peak Height [nm]	17.16	5.447	16.01	12.87
Pit Depth [nm]	3.3	2.788	3.71	3.266

**Table 16** Sample C 10 $\mu$ m

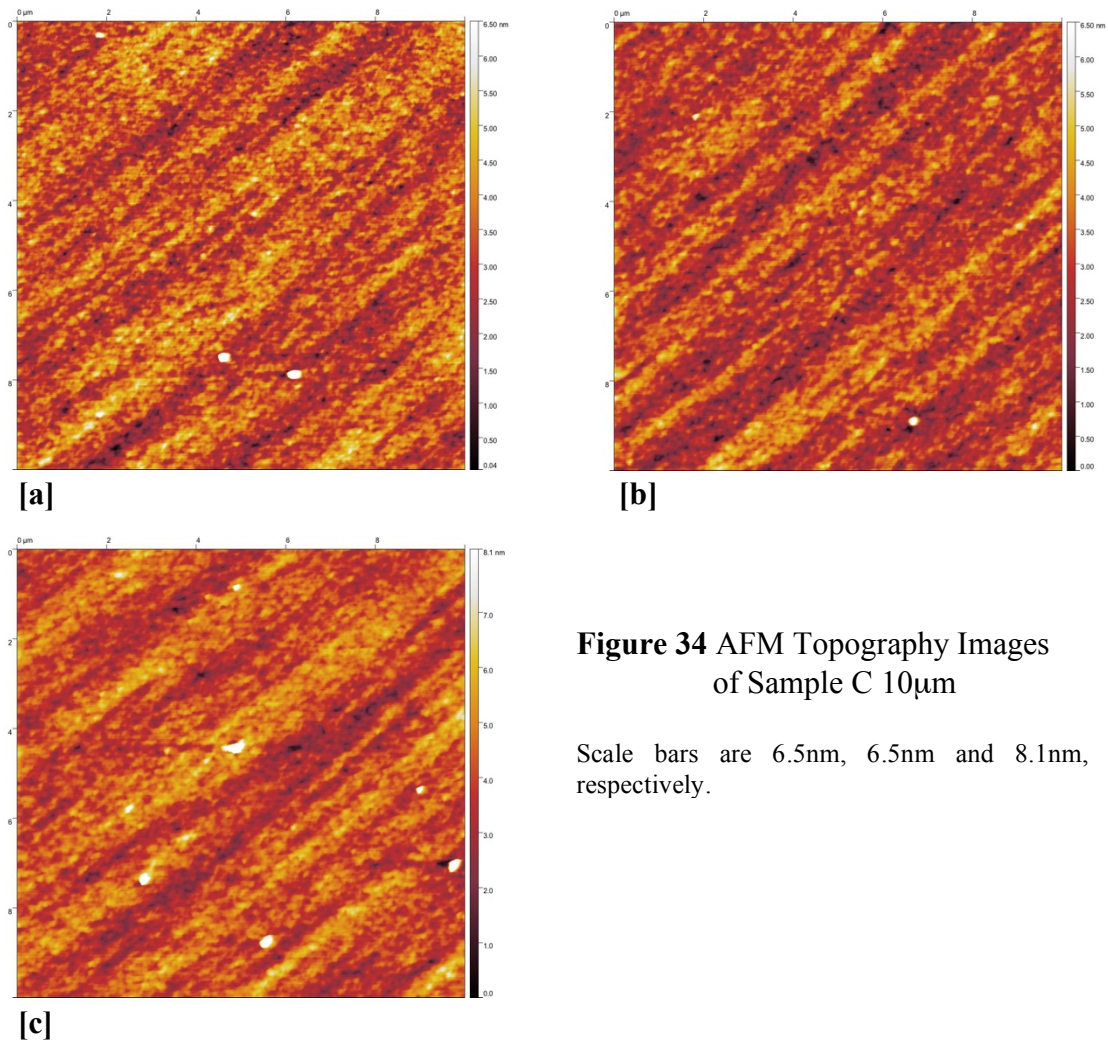


**Figure 34** AFM Topography Images of Sample C 10 $\mu$ m

Scale bars are 6.5nm, 6.5nm and 8.1nm, respectively.

From initial qualitative observations, film thickness and roughness increases when comparing all the samples with each other. The bare quartz reference sample represents the substrate before deposition and shows an averaged roughness of .6253nm, with minimal peaks and pits across the surface. Although it seems that the surface isn't as smooth, these irregularities are from external causes, such as substrate handling or surrounding particles.

For Sample A, the 1 $\mu$ m images, the quantitative values averaged roughness, peak height and pit depth are 0.646nm, 5.156nm and 74.80nm, respectively. The largest peak measured at 8.63nm can be seen in Figure 30(c) at the bottom right hand corner. For 10 $\mu$ m images, quantitative values of averaged roughness, peak height and pit depth were measured to be 0.5283nm, 8.203nm and 2.137nm respectively. The largest peak was measured at 9.95nm in Figure 31(a). When compared to the reference sample, there is a slight contrast difference, but contains overall smoothness.

For Sample B, 1 $\mu$ m images the averaged roughness, peak height and pit depth values were measured at 0.5929nm, 2.654nm and 2.634nm, respectively. The quantitative values for 10 $\mu$ m images were measured at 0.6690nm, 15.76nm and 2.405nm, respectively. Definite surface texture is apparent with increased color contrast, but still "smooth", indicating amorphous film growth.

For Sample C, 1 $\mu$ m images quantitative values of averaged roughness, peak height and pit depth were measured at 1.567nm, 5.733nm and 7.233nm, respectively. The quantitative values for 10 $\mu$ m images were measured at 0.8453nm, 12.87nm, 3.266nm, respectively. Despite having the largest thickness values, Sample C surprisingly has the

lowest RMS roughness values when compared to earlier deposited samples; only to be slightly rougher than the reference sample.

Starting from the bare quartz reference sample to Sample C, the overall progression of film growth is evident. While all samples portray the constant amorphous film characteristics of surface smoothness with atomic irregularity, there are a few notable changes when comparing selected sample images. The first main comparison is between Figure 29 and Figure 31 of Samples A - 1 $\mu\text{m}$  and B - 1 $\mu\text{m}$ . These images are expanded below, in Figure 35 and Figure 36.

It is automatically observed that Sample B - 1 $\mu\text{m}$  contains more roughness than of Sample A - 1 $\mu\text{m}$ , with increased surface texture and color contrast within the 2D images. This difference is highlighted in the 3D images of Sample A and B - 1 $\mu\text{m}$  in Figure 37 and Figure 38. Although there is a definite larger peak for Sample A, as indicated by the z-axis scale bar, the difference in surface roughness, texture and color contrast is significant and indicates increased film growth. To showcase the complete progression of film growth, the 3D image of the bare quartz reference sample and Sample C - 1 $\mu\text{m}$  is also shown in Figure 39 and Figure 40.

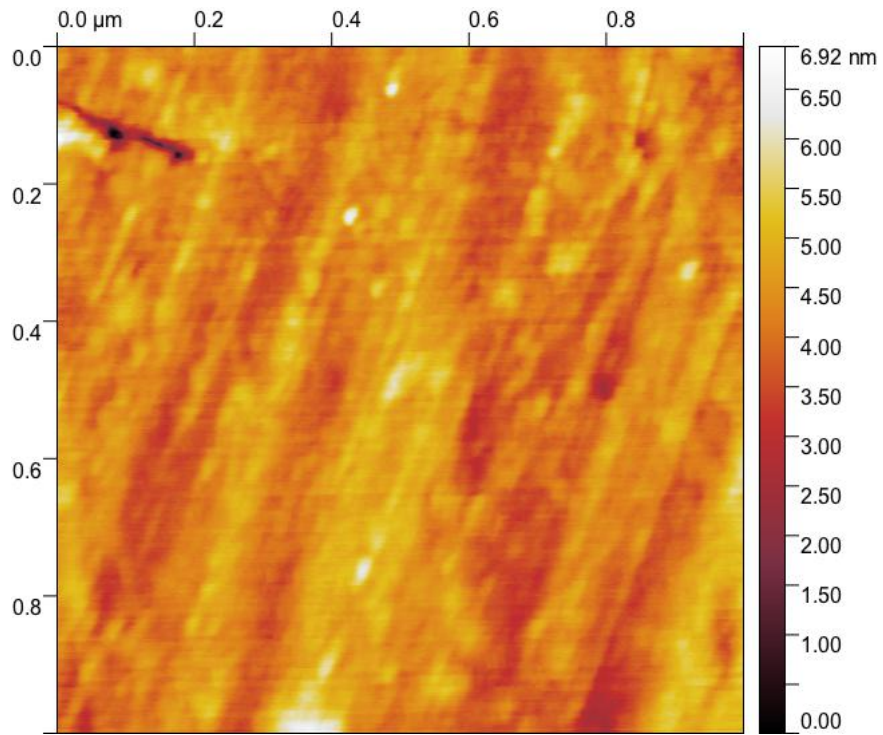


**Figure 35** Magnified Image of Sample A[b] - 1 μm

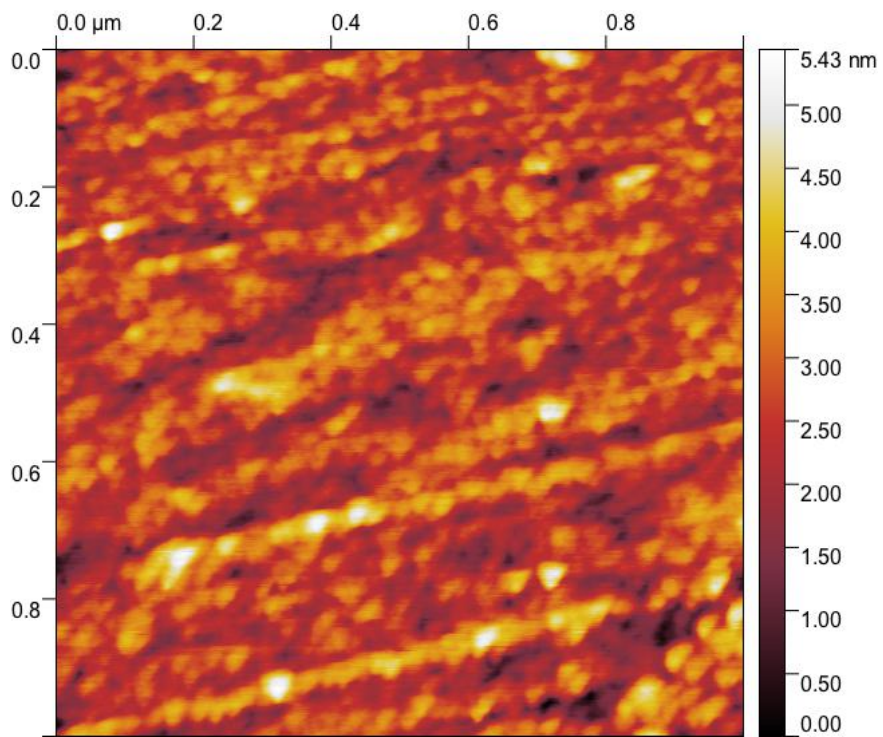


**Figure 36** Magnified Image of Sample B[b] - 1 μm

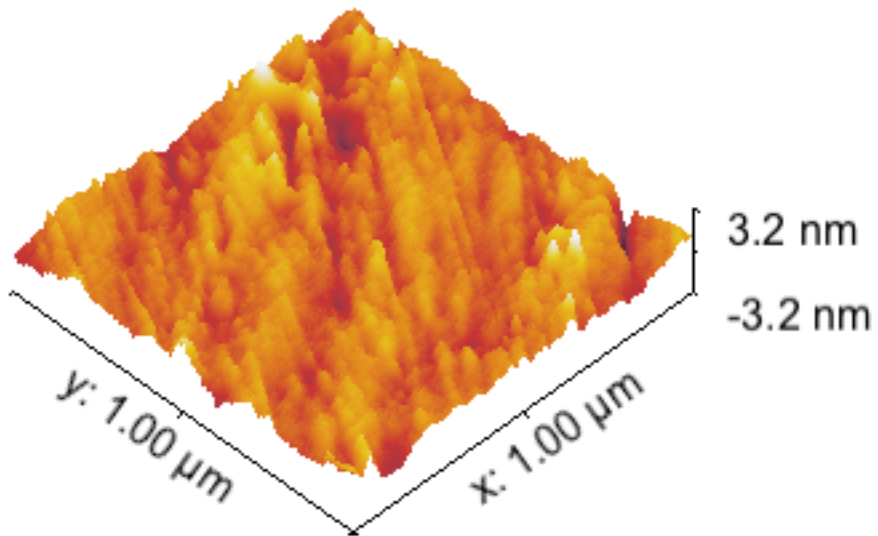


**Figure 37** 3D Image of Bare Quartz Reference [b] - 1 μm

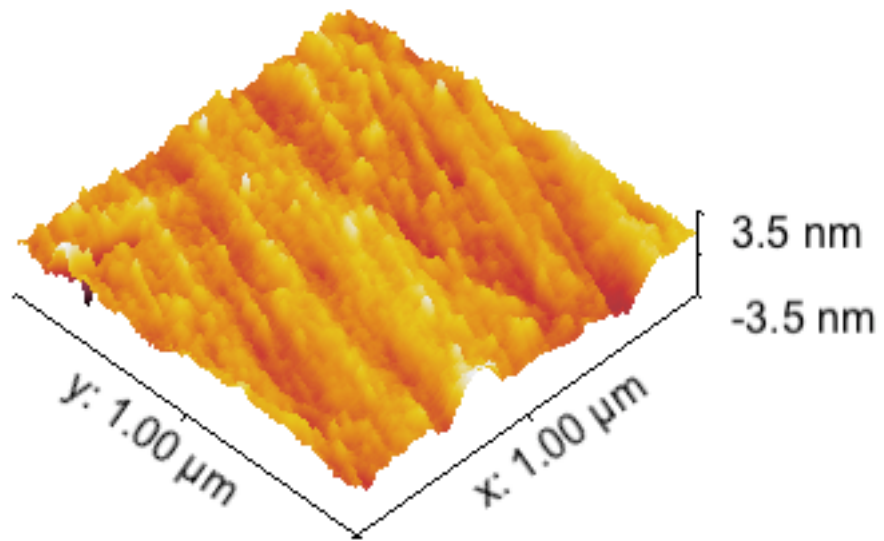


**Figure 38** 3D Image of Sample A[b] - 1 μm

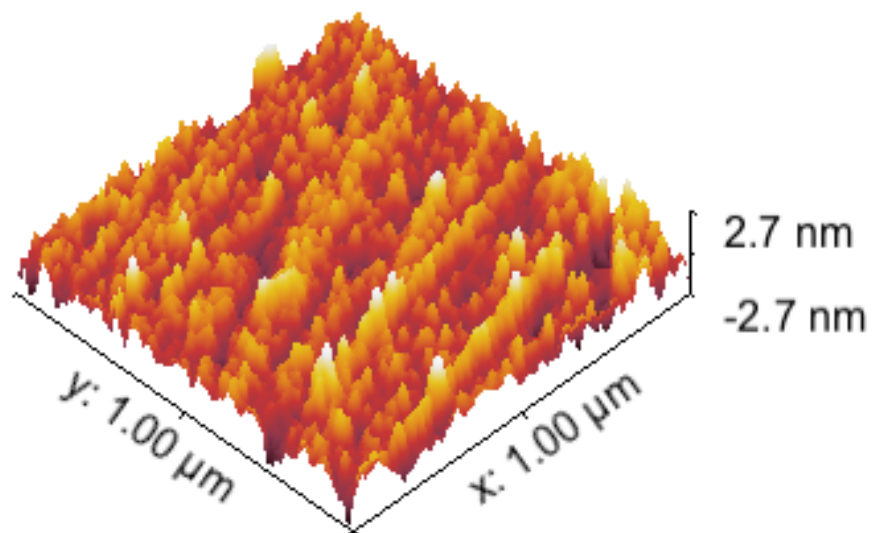


**Figure 39** 3D Image of Sample B[b] - 1 μm

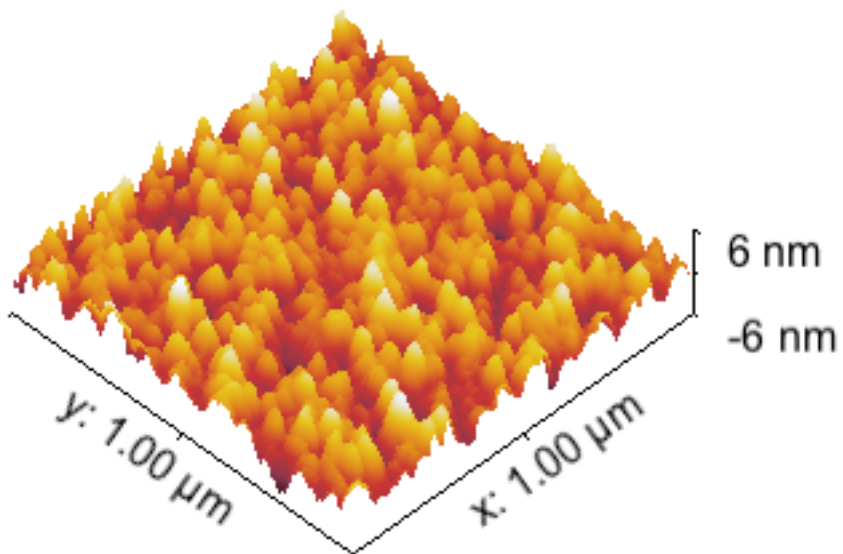


**Figure 40** 3D Image of Sample C[b] - 1 μm

As depicted in the selected 3D ADM images, the progression of film thickness and roughness is fairly linear with respect to deposition time. The slight non-linearity arises between Sample A and B values, where the averaged RMS 1 $\mu$ m roughness value of Sample A is larger than Sample B. This discrepancy is speculated to be caused by two factors: sputtering conditions and deposition time.

Several sputtering conditions are speculated to be the root cause of RMS roughness value discrepancies. The first condition questions the purity of the CuO sputtering target and the subsequent effects. While rated at 99% purity, we did not conduct external tests to confirm its purity. This led to the possibility of non-CuO or Cu particulates present in the deposition chamber and being deposited as well. Furthermore, additional particulates of different sputtering materials were possibly present. While the deposition chamber was thoroughly vacuumed before every experiment, thin film layers from previous depositions were still present across the entire chamber and could have circulated.

In addition to the purity of the CuO sputtering target, the uniformity of its surface could also be the source of data divergences. As the target material is sputtered and depleted, a “racetrack” erosion profile is etched into the surface due to the circular magnetic field concentrating the charged plasma particles. Although RF sputtering reduces this effect when discharging with electrons, the racetrack erosion still occurs but at a reduced rate. This erosion profile affects the sputtering rate by interfering with sputtered ions and resulting in a less uniform deposition.

Another condition that would lead to data inconsistencies is the time allotted for each deposition run. As a target is left to sputter at a specified power, a longer time allotment allows for a constant sputtering rate to occur and result in a more uniform deposition as ions are sputtered at a constant rate. Although RF power was increased incrementally before deposition for all samples, Sample A was only exposed to ions for three minutes, compared to Sample C at 40 minutes. While necessary to deposit the intended thickness, the short amount of time for Sample A is a possible source for the increased roughness when compared to Sample B.

Associated with deposition time, surface energy dynamics is an additional factor to surface roughness. Being the energy correlated with the intermolecular forces at the interface between two media, the surface energy acts as a determining standard when an atom is deposited onto a substrate. As a repeated observation of film growth, depositing atoms naturally cycle through different stages before settling into a lattice site. With increased time, depositing CuO atoms obtain enough energy and time to diffuse to lower energy configurations within three growth modes. The acting growth mode is dependent on multiple factors including binding energy, molecular orientation or free energy levels.

Under cross examination, the quantitative values between AFM images and ellipsometric measurements differ slightly. For clarity, averaged roughness values from AFM 1 $\mu\text{m}$  and 10 $\mu\text{m}$  and ellipsometry are displayed in Table 17, in addition to film thickness and averaged sputtering rate for Samples A-C.

	Sample A	Sample B	Sample C
AFM 1 $\mu$ m Roughness [nm]	0.6461	0.5929	1.567
AFM 10 $\mu$ m Roughness [nm]	0.5283	0.669	0.8453
Ellipsometry Roughness [nm]	0.43	0.51	4.45
Thickness [nm]	3.84	15.49	98.19
Average Sputtering Rate [nm/min]	1.28	1.549	2.45

**Table 17** Comparison of Roughness and Thickness Values of Ellipsometry and AFM

The averaged roughness values from both AFM measurements are consistently larger than ellipsometry roughness measurements. This difference is likely due to the difference in measurement methods; where ellipsometry utilizes light reflectance and transmittance and AFM uses surface peak height and pit depth measurements.

### **3.3 Post Deposition Crystallization**

Comprehensive results of amorphous CuO thin film crystallization with the chevron-tipped laser annealing system is pending. A silicon and quartz wafer of all samples were sent for examination. However, upon initial review and annealing, it was reported that there was a “laser trace” on Samples B and C on Quartz and its images are seen below.

As noted in the following images of initial annealing, laser ablation is a technique of patterning materials by removing material from a surface through irradiation of coupling laser energy. Depending on the energy flux of the laser, the material is heated and can either evaporate, sublimate or convert into plasma. This is headed by the hydrodynamic motion due to thermal expansion when the material surface absorbs laser energy. While it can be used as a film deposition technique, it is also used for materials characterization for semiconductor doping profiling or solid state chemical analysis [12,13]. In both samples, this patterning is indicated at different laser power, with the highest showcasing the most ablation at a scale of 20 $\mu$ m.

#### **Sample B on Quartz**

For Sample B, a set of three images are presented to showcase ablation. The first image displays all irradiation lines across the sample surface, where the second image magnifies the latter irradiation lines. The third image displays the chevron-tipped laser beam used for surface irradiation and is shown last for comparison between both samples.

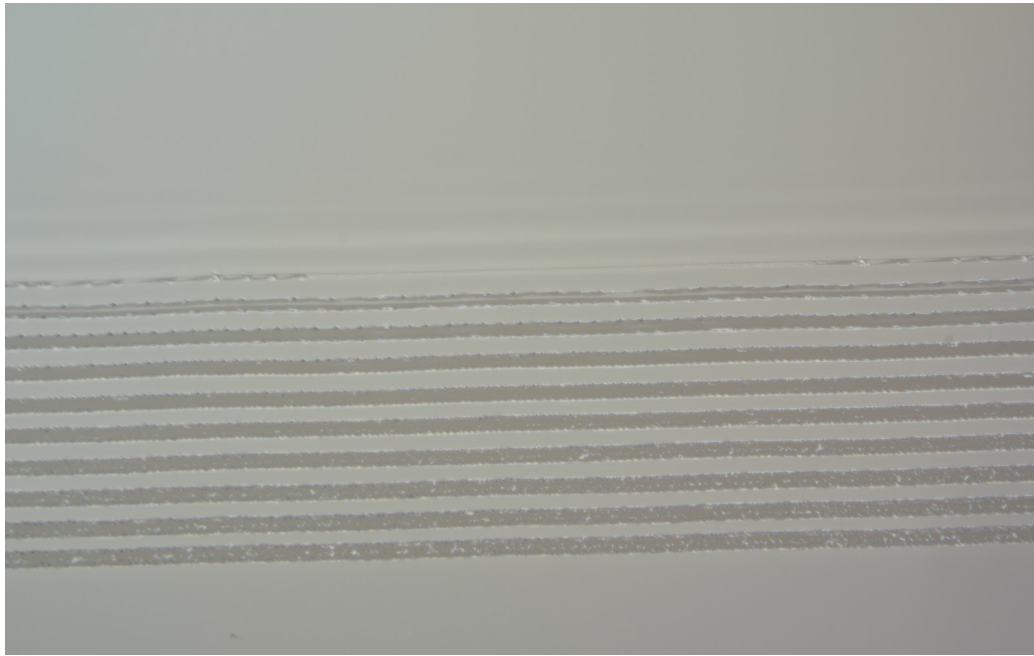


**Figure 41** Total Laser Annealing of Sample B

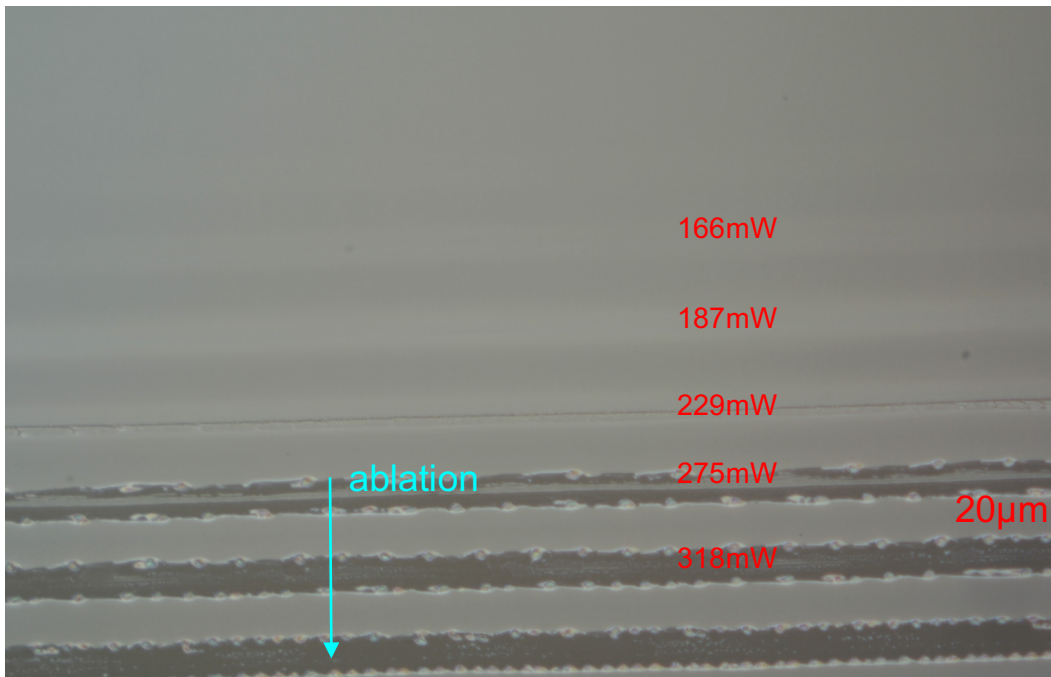


**Figure 42** Magnified Laser Annealing of Sample B with Ablation

### Sample C on Quartz

Similar to Sample B, a set of images are present to showcase laser ablation under the chevron-tipped annealing system. The first image is magnified at the first signs of material patterning at 71mW, where the second image further magnifies to higher laser power. At the highest power of 120mW, ablation is shown, however, the image is unfortunately cutoff.

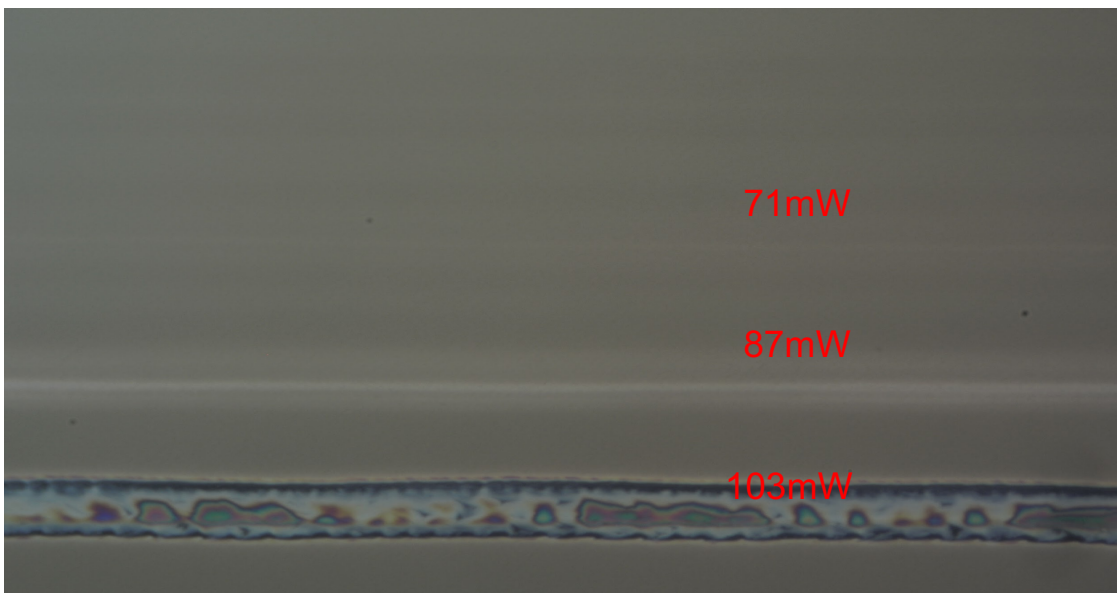


**Figure 43** Laser Annealing of Sample C

At 103mW, there is a distinct marking on the surface of the material and is consistent when compared to previous examples of layer ablation of materials. For Sample C at a measured value of 98.19nm of thickness, this is the required amount of power for surface irradiation.

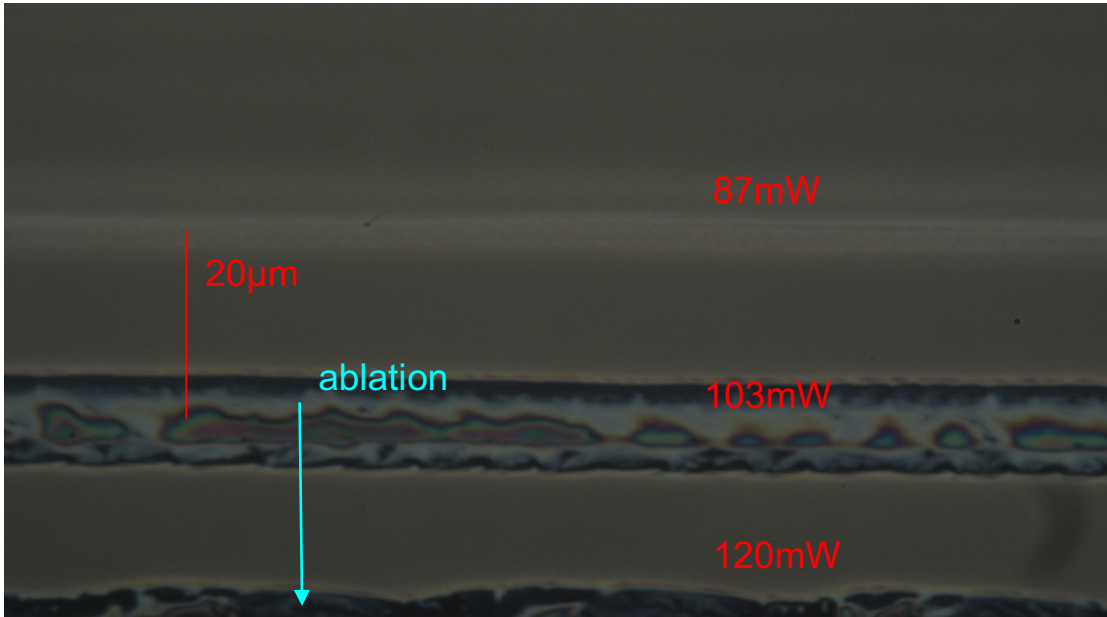


**Figure 44** Magnified Laser Annealing of Sample C

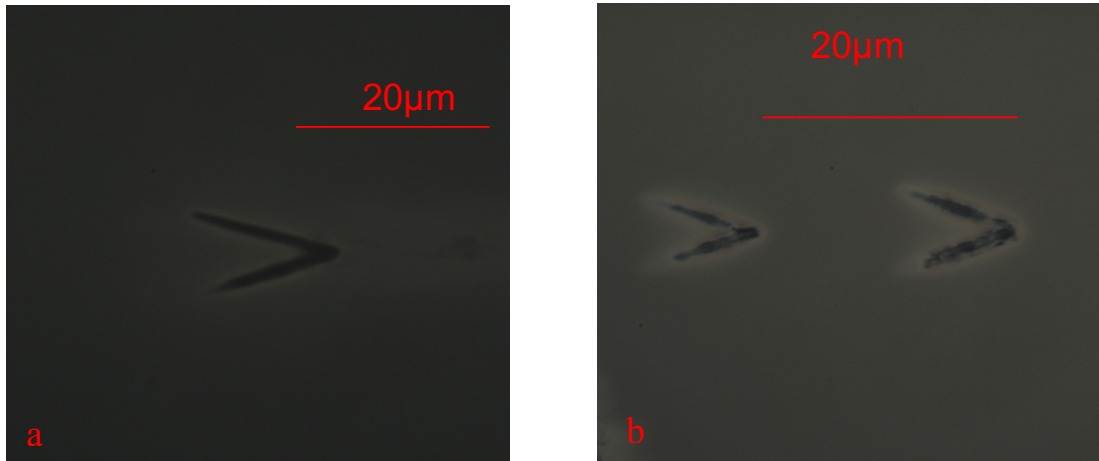


**Figure 45** Surface Irradiation of Chevron-Tipped Laser Beam for (a) Sample B and (b) Sample C

At first glance, the irradiation patterns between Sample B and C are fairly similar. However, it is seen that in Sample C, the point at which ablation is distinctly noted is at a much lower power than in Sample B. Specifically, in Sample C, the point of ablation was reached at 120mW, where in Sample B, that point was reached beyond 318mW, even though the film thickness varies vastly between both wafers. This configuration is also seen when directly comparing the visibility of the irradiation pattern within the chevron-tip shape in Figure 45. This phenomenon could stem from a difference in the average power or repetition rate of the laser pulses. Furthermore, there could have been a difference in surface temperature during irradiation that causes the ablated area to melt at a different rate. However, further characterization and results is pending to determine ultimately whether amorphous CuO thin films were crystallized.

### **Conclusion**

An attempt to successfully fabricate single-crystalline thin film growth on an amorphous surface with a chevron-tipped laser annealing system was executed. Thin film samples were fabricated through sputtering deposition and characterized by ellipsometry and atomic force microscopy. A total of twelve samples of CuO on pre-cleaned quartz and silicon wafers were fabricated at a range of varying film thicknesses at deposition times of 3mins, 10mins, and 40mins.

Post-deposition characterization through ellipsometry, we found the thickness to be 3.84nm, 15.49nm, and 98.19nm for Sample A, B and C, respectively. Furthermore, the

averaged refractive index and extinction coefficient values at 405nm wavelength were found to be 2.74 and 0.75 for Sample A, 2.04 and 0.62 for Sample B and 1.61 and 0.47 for Sample B. In addition, the averaged roughness values were found to be 0.43nm, 0.51nm and 4.45nm, respectively, and confirming the smoothness of an amorphous film. With AFM, we able to confirm qualitatively and quantitatively that the deposited material was an amorphous surface. However, slight discrepancies were also found under cross examination of the surface roughness, specifically with Samples B and C. Furthermore, it was found that the qualitative roughness values for both 1 $\mu$ m and 10 $\mu$ m in Table 17 varied slightly when compared with ellipsometry roughness values. Lastly, results for post-deposition crystallization with the chevron-tipped laser annealing system are in development. However, upon initial images, a laser trace was indicated with laser ablation irradiation patterns at approximately 318mW and 120mW on Samples B and C, respectively. From these recent developments, future experiments includes addition deposition runs with a CuO base layer on quartz and silicon with a silicon-dioxide (SiO<sub>2</sub>) protection cap layer in an effort to provide a stable level of oxygen for CuO during irradiation.

## References

- [1] Wagendristel, Alfred and Wang, Yuming. *An Introduction to Physics and Technology of Thin Films*. New Jersey. World Scientific. 1994.
- [2] J.A. Venables et al., “Nucleation and growth of thin films”. *Rep. Prog. Phys.* **47** (1984) 399
- [3] Eckertová, Ludmila. *Physics of Thin Films*. New York. Plenum Press. 1986.
- [4] A. von Keudell. “Surface processes during thin-film growth.” *Plasma Sources Sci. Technol.* **9** (2000) 455-467. S0963-0252(00)15187-4
- [5] Föll , Helmut. *Science of Uniaxial Deformation*, 2018, [www.tf.uni-kiel.de/matwis/amat/semitech\\_en/kap\\_3/backbone/r3\\_4\\_1.html](http://www.tf.uni-kiel.de/matwis/amat/semitech_en/kap_3/backbone/r3_4_1.html).
- [6] Morris, Jr., J. W. "Defects in Crystals." Chapter 4 in *Materials Science and Engineering: An Introduction*. Wiley, 2013, pp. 76–107.
- [7] P. Sigmund. “Mechanism and Theory of Physical Sputtering By Particle Impact”. *NIM Phys.* **B27** (1987) 1-20.
- [8] “What Is Sputtering?” *AJA International INC*, 2018, [www.ajaint.com/what-is-sputtering.html](http://www.ajaint.com/what-is-sputtering.html).
- [9] W. Yeh, S. Yamazaki, A. Ishimoto, S. Morito. *J. Phys. Soc. Jpn.* Vol. 9 (2016) 025503
- [10] A.R. Forouhi and I. Bloomer. “Optical Dispersion Relations for Amorphous Semiconductors and Amorphous Dielectrics.” *Phys. Review B.* Vol. 34. 10. (1986)
- [11] Ambios Technology Co. “Q-Scope 250/400 Nomad”. *Operator’s Manual*. California. 2007. Print.
- [12] Schneider C.W., Lippert T. (2010) Laser Ablation and Thin Film Deposition. In: Schaaf P. (eds) *Laser Processing of Materials*. Springer Series in Materials Science, vol 139. Springer, Berlin, Heidelberg
- [13] Phipps, C. R., *Laser Ablation and its Applications*, Springer, New Mexico. 2007. Print.

- [14] H. Kurz. “Fundamentals of Pulse Laser Annealing”. *Advances of Solid State Physics. Festkörperprobleme 23*, Springer. (2007) pp 115-140
- [15] J.J.P. Bruines, R.P.M van Hal, B.H. Koek, M.P.A. Vieggers and H.M.J. Boots. “Between explosive crystallization and amorphous regrowth: Inhomogeneous solidification upon pulse-laser annealing of amorphous silicon”. *Appl. Phys. Lett.* 50 , 507 (1987); doi: 10.1063/1.98142
- [16] W. Yeh. “Fabrication of single crystalline stripe in Si and Ge film on rolled flexible glass substrate by UV cw micro-chevron laser beam”, *Proc. SPIE 10349, Low-Dimensional Materials and Devices 2017*, 103490R
- [17] Jimenez, J. and Tomm, J.W. *Spectroscopic Analysis of Optoelectron Semiconductors*. Springer. 2016.
- [18] K. Chen, et. al. “Direct Growth of Single-Crystalline III-V Semiconductors on Amorphous Substrates.” *Nature Communications.* 7:10502 (2016). DOI:10.1038.
- [19] M. Çelikkilek, A. E. Ersundu and S. Aydın (April 27th 2012). “Crystallization Kinetics of Amorphous Materials”, *Advances in Crystallization Processes*, Yitzhak Mastai, IntechOpen, DOI: 10.5772/35347.
- [20] Ekuma, Chinedu & Anisimov, Viadimir & Moreno, Juana & Jarrell, M. (2013). “Electronic Structure and Spectra of CuO”. *Physics of Condensed Matter.* 87. 10.1140/epjb/e2013-40949-5.
- [21] Z. Zhang. And M.G. Lagally. (1997). “Atomic Processes in the Early Stages of Thin-Film Growth”. *Science.* Vol. 276. 377-383.